Alma Mater Studiorum – Università di Bologna

DOTTORATO DI RICERCA IN
NANOSCIENZE PER LA MEDICINA E PER L'AMBIENTE

Ciclo *XXXV*

Settore Concorsuale: 03/B1 - FONDAMENTI DELLE SCIENZE CHIMICHE E SISTEMI INORGANICI

Settore Scientifico Disciplinare: CHIM03 – CHIMICA GENERALE E INORGANICA

FLUOROGENIC HYALURONAN-BASED PROBE: CHARACTERIZATION AND USE IN ADVANCED MICROSCOPY

Presentata da: Matteo Cingolani

Coordinatore Dottorato
Prof. Dario Braga

Supervisore
Prof. Luca Prodi

Co-Supervisore
Prof. Damiano Genovese

Esame finale anno 2023

ABSTRACT

In the last few decades, nanomaterials have been widely recognised as powerful sensing tools due to their unique properties. The development of new nanomaterials and the understanding of their behaviour have been explored in many fields joining forces from different knowledges in science and making them extremely promising for fundamental and practical applications. Among all, the application of nanomaterials in biomedical research and most recently in the environmental one have opened the fields of nanomedicine and nanoremediation. Furthermore, sensing methods based on fluorescence optical probe are generally requested among other technique for their selectivity, sensitivity and easy handling of the sample. However, most imaging methods in literature, both diffraction limited and super-resolution ones, rely on an effective covalent labelling of the system with fluorescent dye or ligand/receptor coupled moieties to study surface properties and topography. When systems under analysis struggle to be easily functionalized with fluorescent moieties this is a major limitation for different application. Therefore, the main aim of this Ph.D thesis was to synthetise a biocompatible fluorogenic hyaluronan probe

(HA) polymer functionalised with a rhomadine B (RB) moiety and study its behaviour as an optical probe with different materials with microscopy technique. A derivatization of HA with RB (HA-RB) was successfully obtained and a photophysical characterization as been provided showing a particular fluorescence mechanism of the probe. To prove their sensing ability towards nanomaterial, the interaction with different lab-grade micro and nanoplastics was tested in water. It has been demonstrated that thank to the peculiar photophysical behaviour of the probe nanoplastics can be detected with confocal microscopy and more interestingly their nature can be discriminated based on the fluorescence lifetime decay with FLIM microscopy. After, it has been studied the interaction of a model plant derived metabolic enzyme GAPC1 undergoing oxidative-triggered aggregation with the HA-RB probe. Interestingly, compared to classical turbidity scattering measurement, the emission signal due to the progressive aggregation starts to rise much earlier than the scattering, during the so called lag-time. This means that the probe is interacting with oligo/pre-aggregates of the protein and it is thus able to reveal them on the contrary of what happens in presence of Thioflavin-T, a model dye for

protein aggregates detection. Hence the ability of HA-RB stems not from the technique (fluorescence vs scattering) but from the probe itself, highlighting therefore the importance of the polymeric nature and of the fluorogenic mechanism of the probe. Moreover, nanoparticle tracking analysis (NTA) experiment with homemade optical setup demonstrate that the probe is able to interact with the small pre-aggregates in the early stage of the aggregation kinetic, as suggested by the fluorescence cuvette essay. At the end, we explored the possibility to apply the probe in a super resolution microscopy technique, PALM, exploiting the aspecific interaction of the HA-RB to reach the optimal condition for the technique to characterize the surface topography of PTFE polydisperse microplastics. Optimal condition were reached easily at high concentration of the probe (70 nM) which is the opposite you should except from this technique were a 0.5-5 nM is always advisable to have a good blinking of the emitters. This can be explained with the polymeric nature of the probe which with this technique was able to reveal features of PTFE surface under the diffraction limit (< 250 nm).

Contents

Chapter 1-General introduction

1.1 Interfaces and Interaction: how to explore the nanoworld

As we proceed down along the scale of dimensions, the understanding of the interfaces and phase separation represent a key factor to recognize the properties of a system and how to interact with them.

This become more relevant in the nanostructured materials since there are intrinsically characterized by an high surface-to-volume ratio and peculiar physical-chemical characteristics, as also defined by the European Commission [1]. In fact, in this dimensional range, surfaces become intense topic of study in all the field of the science as they play a crucial role in chemical, physical and biological processes involving nanostructured materials interactions.

In the last decades, the understanding of the forces involved have already led to the development of nanotechnology and nanomaterials for a plethora of

applications in i.e., energy conversion [2], molecular recognition and signal transduction [3], *in vivo* and *in vitro* diagnostic and therapy [4] and environmental control [5].

A large effort has been employed in the comprehension of the interactions and the relationship intercurrent between properties and structure of the nanomaterials in order to rationally design the properties of new nanomaterials.

For example, a consistent part of the literature about nanomaterials are meant to have a biomedical application and, most recently, a lot of studies are focused on environmental application.

For those applications, one of the most important aspects explored is the detection of the system of interest itself. Physically, this implies a surface, a region that separates two different phases and, chemically, what is present on that surface that can be used to interact with a rationally designed sensor. In this contest, among all the tuneable properties, specificity and sensitivity become a main aspect for creating a sensor and this could be realized in different ways.

1.2 Nanomaterials for biomedical and environmental applications

When the dimensionality of a material is confined in the nanometric range, its physical and chemical properties change drastically from the bulky material and in this situation the physical phenomena are governed by quantum mechanics. In addition, another peculiar feature of the material, independent from shape or composition is a large surface/volume ratio-which influences mechanical, optical and magnetic properties.

The development of new nanomaterials and the understanding of their behaviour have been explored especially towards the two big application fields of biomedical and, more recently, environmental control.

In this context, nanomaterials can be divided in two groups depending on their chemical nature: inorganic and organic nanomaterials. Inorganic nanomaterials includes noble metal quantum dots (Au, Pt, Ag), oxide-based (i.e., Fe_3O_4 as in magnetic nanoparticles), carbon-based (nanotubes, fullerenes, c-dots), semiconductor, silica-based nanoparticles [6] and AIE-gen materials [7]. Organic

nanomaterials can include biocompatible polymers like poly (lactic-co-glycolic acid), hyaluronic acid, chitosan, polylactic acid forming nanoparticles [8], dendrimers and liposomes [9].

Of course, given this general separation, literature is flourishing of many nanomaterials conjugating the organic and inorganic nature, joining the peculiar properties of both sides to face the complexity of the interactions in the biomedical and environmental fields [10]. Consequently, the understanding of the relationship between the nanomaterial activity with their structure opens to the possibility of rationally design and tune their properties.

1.2.1 Biomedical application: *Nanomedicine*

Many features are responsible for the success of nanomaterials in biomedical application. First to mention above all is their size which is comparable to many biological cellular system and biomolecules, letting them be potentially integrated into cellular uptake processes with different purposes from diagnosis to therapy. This property is strengthened when the nanomaterial is

designed in order to maximize its biocompatibility [11] which is possible by joining inorganic and organic nanomaterials avoiding most of unwanted effects like (i.e. immunogenic [12] response, protein corona formation [13]). This common strategy makes possible to extensively study their biodistribution and bioavailability and their pharmacokinetics. Also, it has been highlighted how several nanomaterials has a great stability in physiological condition ensuring stable action through time, effective bio-distribution and accumulation and protection of drugs/probes load from external environment actions.

Indeed, the size of nanomaterials is perfect to exploit the so-called Enhanced Permeability and Retention (EPR) effect, a phenomenon present in many types of cancer diseases. Typically, cancer cells usually exhibit higher nutrients demand and hypoxia state which thus requires a higher oxygen demand from the blood stream. This leads to the creation of a new blood vessels (a process called angiogenesis) in the proximity of the ill tissues. This new vascularization system is not as tight as a healthy one; on the contrary presents looseness and intricate leaking blood vessel. Exploiting this permeability, nanomaterials are big

enough to passively enter and accumulate in the tumor tissues and be retained for a longer time. Typically, a strong EPR effect can be achieved using nanomaterials ranging from 10 to 200 nm [14].

Together with the size, the nature and charge of the surface play an important role especially in the uptake and clearance process [15]. Whereas positively charged nanomaterials exhibits electrostatic interaction with the negatively charged cell membrane and much higher uptake *in vitro* respect to neutral and negatively charged analogous, *in vivo* situation could be quite different. In this case, the positive nanomaterial can be affected by non-specific surface absorption of serum proteins (immunoglobulins, fibrinogen, albumin, apolipoproteins) forming the so-called protein corona (PC) [16]. The PC formation alters the size of the nanoparticles and can cause physical destabilization and aggregation. In addition, PC can ease nanomaterial recognition by macrophages and the immune system triggering a fast clearance response and, for the same reason, it can sensitize the immunogenic response and toxicity. On the other side, negatively charged nanomaterials are less affected from the PC

formation and generally are present for longer time in the blood [17].

Furthermore, the unmet versatility of nanomaterials is also due to the possibility to chemically modify their surface with several methods. Indeed, they constitutes a powerful platform to be engineered with well-known and easy to perform techniques: biomolecule conjugation (antibody, oligonucleotides, polypeptides), biocompatible passivation (PEG, PLGA and copolymer), releasable loading (drugs, probes), fluorescent probes for optical sensing [18]. With this powerful set of tools is possible to tune the half-life allowing the synthesis of new system to active targeting and therefore providing high specificity and sensitivity, thus increasing the effectiveness. Indeed, active targeting is a strategy to specifically make the nanomaterials perform their function upon an active interaction between biomolecules and receptors on the cells surface. In order to achieve such results, a deep comprehension of the nature of the surfaces interaction and the recognition molecules involved are quite important.

1.2.2 Environmental applications: *Nanoremediation*

In the last century thanks to scientific discoveries and great technologies advancements, the human society had an unmet and extensive progress in industrialization. As consequence, this phenomenon brought also important problems for all the biosphere with a pollution phenomenon whose entity is dramatically worsened throughout the last decades concurring to the current worldwide climate crisis. This huge environmental pollution constitutes an enormous ecological risk with the release and accumulation of big amount of toxic species in air, water, and soil with alarming consequences for all the living organism and rising concerns also for human health. Thus, there is a crucial need to develop systems and methodology for an efficient environmental remediation. Remediation terminology is mainly associated with environment by means of all the processes involved in detection and the removal of pollutants and toxic contaminants from soil, atmosphere, groundwater, sediments, and hydrosphere. Since there different pollutants can be found most likely in specific environment respect to another, the complexity of

remediation in different environment has been faced with different approaches. They are divided in three main groups: physical (soil washing and flushing, land-farming, soil vapour extraction), chemical (stabilization of pollutants to a less toxic form with oxidising species, metal-chelating agents, chemical precipitation, or photodegradation) and biological remediation (microbial and phytoremediation). However, current classical approaches are quite laborious, considerably expensive and time consuming. Especially, bioremediation has some drawbacks intrinsically linked to the use of organisms which need optimized conditions for their growth, whose obtainment is not instantaneous. Moreover, in the last few years new concerns arise from contaminants referred as emerging pollutants (EP)[19]. They consist in chemical substances detected in the environment which are not well regulated and consequently not included in routine monitoring programmes and whose fate, behaviour and toxicological effects on environment and human health are not well understood. They are in form of pesticides, industrial chemicals, surfactants, personal care products and pharmaceuticals that are consistently being found in

groundwater, surface water, municipal wastewater, drinking water, and food sources. In some cases, release of emerging pollutants to the environment has likely occurred for a long time but may not have been recognized until new detection methods were developed. To overcome the inefficiency of classical methods, application of nanotechnology has started to be explored to achieve the most radical changes in the field of detection and environmental remediation [20]. For example, non-steroidal anti-inflammatory drugs (NSAIDs) are one of the most used active principle in drugs formulation and the lack of regulation and methodology on its lifecycle (synthesis, removal, storage and disposal of the waste) lead to their increasing presence in the aquatic environment [21]. For this class of drugs, many fluorescent nanostructured systems have been proposed such as Cd/S quantum dots (QDs) or CdSe/ZnS QDs, polymer imprinted carbon dots, chitosan-stabilized Ag nanoparticles and also H-bond interaction with small molecules [22]. Furthermore, one of the most recent globally concerning EPs are those related to the phenomenon of micro and nano plastics pollution [23,24]. This theme is particularly taken

into consideration, EU and global organizations have already set the objective to determine new methodology for sensing and removal of plastic debris in the environment in the next few years. Also in this case the literature is flourishing of new system and methods for detection such metal organic framework (MOFs) [25], Superparamagnetic iron oxide nanoparticles (SPIONs) [26], carbon nanotubes (CNTs) [27], chitin [28].

1.3 Optical Probes: Fluorescent Nanomaterials

One of the more interesting properties of nano-probes exploited in biomedical and environmental applications rely on their optical properties. An optical nano-probe is a system containing a recognition element linked to an optical transducer able to generate a signal related to the presence of a target analyte. The probes can work in a label free [29] or with labelling approach. The latter, through an optimal choice of the recognition element for the specific analyte, relies on the generation of a colorimetric or luminescent signal. Specifically, the optical properties that can be exploited are fluorescence, phosphorescence,

chemiluminescence, electrochemiluminescence, thermo-chemiluminescence, absorbance and reflection. The most common probes are the ones based on fluorescence, exploiting the changes of different properties such as emission intensity, lifetime, and anisotropy. These properties can be affected through the modulation of energy, electron or proton transfer processes, the formation of excimers and exciples, or aggregation induced emission processes. The detection ability of the probe is evaluated upon the variation of a fluorescent moiety properties upon interaction with the analyte in its environment so that it is important to properly design the probe, taking into account its photochemical and chemical stability. Organic dyes and transition metal complexes are usually used since the easiness to tune their properties. They are usually composed with an extended π-system with a variety of functional groups. Their electromagnetic spectrum can be tuned changing the extension and the functionalization of the π-system. Hydrophobicity of the probe is also tuneable and relevant especially for biomedical and environmental application. Although these parameters can be tuned by changing the extension of the π-system or the functional

groups on the organic dyes, in many cases coupling the optical potentiality of the probe with nanomaterials can be a successful strategy. Nanomaterials have been presenting fundamental instruments for an easy engineering and an unmet tuning of sensing systems based on interaction phenomena occurring at the nanoscale. In fact, nanomaterials can be used as a signal amplification platform thanks to their intrinsic properties, and they can improve the efficiency of the interaction event in the recognition and detection processes.

1.4 Hyaluronic Acid

In the family of glycosaminoglycan, we can find the hyaluronic acid (HA)[30]. It is a biopolymer whose monomeric unit is a disaccharides composed by N-acetyl-D-glucosamine and D-glucuronic acid, linked by β(1-3) and β(1-4) glycosidic bonds, with a molecular weight ranging from less than 10 to 104 KDa [31]. Since the pK_a of the carboxylic residue in the HA is between 3 and 4, In physiological condition (pH = 7) it is easily ionized. Consequently, the HA can be found in its polyanion form in *random coil* conformation stabilized by intramolecular H-

bonds. Hyaluronic acid is a macromolecule present in high quantity in mammalians and it is ubiquitarian in all the organisms where it takes part directly in many processes, especially in tissues with structural, biomechanical and barrier functions due to the steric hinderance of its network. Although for long time HA has been considered as a simple filler of extracellular matrix (ECM), research conducted in the recent years highlighted its active role of signal molecule for the homeostasis of many cellular processes (morphogenesis, tissue remodelling, inflammation and pathogenesis). Through the interaction with different proteoglycans and linking proteins the HA maintains the structural integrity of the ECM. On the other hand, as signalling molecule, HA interacts with different cellular surfaces, proteins and receptors such as transmembrane receptor cluster determinant 44 (CD44) and receptor for hyaluronate-mediated motility (RHAMM)[32]. These aspects have attracted interest for the interaction potential of HA with nanomaterials in nanomedicine applications, in the synthesis of Hyaluronic acid-based nanoparticles for therapeutic and sensing.

1.4.1 Hyaluronic acid for Nanomedicine and Nanoremediation

The ability of hyaluronic acid to interact with cells and biological systems brought to the production of extensive literature on hyaluronic acid used as probe. In our group, derivatized hyaluronic acids have been proved to interact with soft shell nanoparticles with interesting results [33]. This has attracted our interest to investigate and explore the possible new applications of hyaluronic based probes and its versatility towards nanomaterials of biological and environmental interest. Hence, in this work we explore the potentialities of a probe based on hyaluronic acid as a flexible tool for the detection and characterization of different nanomaterials. In particular, the probe involved consist in fluorogenic hyaluronan probe whose synthesis and sensing mechanism will be discuss extensively in the following chapters.

Indeed, interesting results have been achieved using HA_RB as a probe to detect micro-plastics and to obtain information on their dimensions and chemical nature in aqueous samples. Moreover, an interaction between hyaluronic acid and protein aggregates have been observed, allowing to monitor live the aggregation kinetic since the early stage.

1.5 References

[1] G. Lidén, The European commission tries to define nanomaterials, Ann. Occup. Hyg. 55 (2011) 1–5. https://doi.org/10.1093/annhyg/meq092.

[2] Q. Zhang, E. Uchaker, S.L. Candelaria, G. Cao, Nanomaterials for energy conversion and storage, Chem. Soc. Rev. 42 (2013) 3127–3171. https://doi.org/10.1039/c3cs00009e.

[3] J. Wang, Nanomaterial-based amplified transduction of biomolecular interactions, Small. 1 (2005) 1036–1043. https://doi.org/10.1002/smll.200500214.

[4] J.U. Menon, P. Jadeja, P. Tambe, K. Vu, B. Yuan, K.T. Nguyen, Nanomaterials for photo-based diagnostic and therapeutic applications, Theranostics. 3 (2013) 152–166. https://doi.org/10.7150/thno.5327.

[5] A. Aghababai Beni, H. Jabbari, Nanomaterials for Environmental Applications, Results Eng. 15 (2022) 100467. https://doi.org/10.1016/j.rineng.2022.100467.

[6] S.E. Lohse, C.J. Murphy, Applications of colloidal inorganic nanoparticles: From medicine to energy, J. Am. Chem. Soc. 134 (2012) 15607–15620. https://doi.org/10.1021/ja307589n.

[7] Y. Liu, X. Guan, Q. Fang, Recent advances in AIEgen-based crystalline porous materials for chemical sensing, Aggregate. 2 (2021) 1–15. https://doi.org/10.1002/agt2.34.

[8] A. Gagliardi, E. Giuliano, E. Venkateswararao, M. Fresta, S. Bulotta, V. Awasthi, D. Cosco, Biodegradable Polymeric Nanoparticles for Drug

Delivery to Solid Tumors, Front. Pharmacol. 12 (2021) 1–24. https://doi.org/10.3389/fphar.2021.601626.
[9] Y. Malam, M. Loizidou, A.M. Seifalian, Liposomes and nanoparticles: nanosized vehicles for drug delivery in cancer, Trends Pharmacol. Sci. 30 (2009) 592–599. https://doi.org/10.1016/j.tips.2009.08.004.
[10] A. Luchini, G. Vitiello, Understanding the nano-bio interfaces: Lipid-coatings for inorganic nanoparticles as promising strategy for biomedical applications, Front. Chem. 7 (2019) 1–16. https://doi.org/10.3389/fchem.2019.00343.
[11] M. Jiao, P. Zhang, J. Meng, Y. Li, C. Liu, X. Luo, M. Gao, Recent advancements in biocompatible inorganic nanoparticles towards biomedical applications, Biomater. Sci. 6 (2018) 726–745. https://doi.org/10.1039/c7bm01020f.
[12] T.R. Kyriakides, A. Raj, T.H. Tseng, H. Xiao, R. Nguyen, F.S. Mohammed, S. Halder, M. Xu, M.J. Wu, S. Bao, W.C. Sheu, Biocompatibility of nanomaterials and their immunological properties, Biomed. Mater. 16 (2021) 1–49. https://doi.org/10.1088/1748-605X/abe5fa.
[13] S. Ma, C. Gu, J. Xu, J. He, S. Li, H. Zheng, B. Pang, Y. Wen, Q. Fang, W. Liu, J. Tian, Strategy for Avoiding Protein Corona Inhibition of Targeted Drug Delivery by Linking Recombinant Affibody Scaffold to Magnetosomes, Int. J. Nanomedicine. 17 (2022) 665–680. https://doi.org/10.2147/IJN.S338349.
[14] J. Wu, The enhanced permeability and retention (Epr) effect: The significance of the concept and

methods to enhance its application, J. Pers. Med. 11 (2021). https://doi.org/10.3390/jpm11080771.
[15] C. Allen, T.A. Qiu, S. Pramanik, J.T. Buchman, M.O.P. Krause, C.J. Murphy, Research highlights: investigating the role of nanoparticle surface charge in nano-bio interactions, Environ. Sci. Nano. 4 (2017) 741–746. https://doi.org/10.1039/c7en90014g.
[16] R. Rampado, S. Crotti, P. Caliceti, S. Pucciarelli, M. Agostini, Recent Advances in Understanding the Protein Corona of Nanoparticles and in the Formulation of "Stealthy" Nanomaterials, Front. Bioeng. Biotechnol. 8 (2020) 1–19. https://doi.org/10.3389/fbioe.2020.00166.
[17] J.Y. Oh, H.S. Kim, L. Palanikumar, E.M. Go, B. Jana, S.A. Park, H.Y. Kim, K. Kim, J.K. Seo, S.K. Kwak, C. Kim, S. Kang, J.H. Ryu, Cloaking nanoparticles with protein corona shield for targeted drug delivery, Nat. Commun. 9 (2018) 1–9. https://doi.org/10.1038/s41467-018-06979-4.
[18] R.A. Sperling, W.J. Parak, Surface modification, functionalization and bioconjugation of colloidal Inorganic nanoparticles, Philos. Trans. R. Soc. A Math. Phys. Eng. Sci. 368 (2010) 1333–1383. https://doi.org/10.1098/rsta.2009.0273.
[19] V. Geissen, H. Mol, E. Klumpp, G. Umlauf, M. Nadal, M. van der Ploeg, S.E.A.T.M. van de Zee, C.J. Ritsema, Emerging pollutants in the environment: A challenge for water resource management, Int. Soil Water Conserv. Res. 3 (2015) 57–65. https://doi.org/10.1016/j.iswcr.2015.03.002.
[20] A.P. Ingle, A.B. Seabra, N. Duran, M. Rai,

Nanoremediation: A New and Emerging Technology for the Removal of Toxic Contaminant from Environment, Elsevier Inc., 2014. https://doi.org/10.1016/B978-0-12-800021-2.00009-1.

[21] P. Izadi, P. Izadi, R. Salem, S.A. Papry, S. Magdouli, R. Pulicharla, S.K. Brar, Non-steroidal anti-inflammatory drugs in the environment: Where were we and how far we have come?, Environ. Pollut. 267 (2020) 115370. https://doi.org/10.1016/j.envpol.2020.115370.

[22] G.M. Romano, L. Mummolo, M. Savastano, P. Paoli, P. Rossi, L. Prodi, A. Bencini, Polyamine receptors containing anthracene as fluorescent probes for ketoprofen in H2O/EtOH solution, Chem. Commun. 58 (2022) 7022–7025. https://doi.org/10.1039/d2cc01107g.

[23] Z. Wang, Y. Zhang, S. Kang, L. Yang, H. Shi, L. Tripathee, T. Gao, Research progresses of microplastic pollution in freshwater systems, Sci. Total Environ. 795 (2021) 148888. https://doi.org/10.1016/j.scitotenv.2021.148888.

[24] E.L. Ng, E. Huerta Lwanga, S.M. Eldridge, P. Johnston, H.W. Hu, V. Geissen, D. Chen, An overview of microplastic and nanoplastic pollution in agroecosystems, Sci. Total Environ. 627 (2018) 1377–1388. https://doi.org/10.1016/j.scitotenv.2018.01.341.

[25] Y.J. Chen, Y. Chen, C. Miao, Y.R. Wang, G.K. Gao, R.X. Yang, H.J. Zhu, J.H. Wang, S.L. Li, Y.Q. Lan, Metal-organic framework-based foams for efficient microplastics removal, J. Mater. Chem. A. 8 (2020) 14644–14652.

https://doi.org/10.1039/d0ta04891g.
[26] M. Sarcletti, H. Park, J. Wirth, S. Englisch, A. Eigen, D. Drobek, D. Vivod, B. Friedrich, R. Tietze, C. Alexiou, D. Zahn, B. Apeleo Zubiri, E. Spiecker, M. Halik, The remediation of nano-/microplastics from water, Mater. Today. 48 (2021) 38–46. https://doi.org/10.1016/j.mattod.2021.02.020.
[27] Y. Tang, S. Zhang, Y. Su, D. Wu, Y. Zhao, B. Xie, Removal of microplastics from aqueous solutions by magnetic carbon nanotubes, Chem. Eng. J. 406 (2021) 126804. https://doi.org/10.1016/j.cej.2020.126804.
[28] C. Sun, Z. Wang, H. Zheng, L. Chen, F. Li, Biodegradable and re-usable sponge materials made from chitin for efficient removal of microplastics, J. Hazard. Mater. 420 (2021) 126599. https://doi.org/10.1016/j.jhazmat.2021.126599.
[29] V.R. Samuel, K.J. Rao, A review on label free biosensors, Biosens. Bioelectron. X. 11 (2022) 100216. https://doi.org/10.1016/j.biosx.2022.100216.
[30] A.J. Day, G.D. Prestwich, Hyaluronan-binding proteins: Tying up the giant, J. Biol. Chem. 277 (2002) 4585–4588. https://doi.org/10.1074/jbc.R100036200.
[31] J.M. Cyphert, C.S. Trempus, S. Garantziotis, Size Matters: Molecular Weight Specificity of Hyaluronan Effects in Cell Biology, Int. J. Cell Biol. 2015 (2015). https://doi.org/10.1155/2015/563818.
[32] S. Misra, V.C. Hascall, R.R. Markwald, S. Ghatak,

Interactions between hyaluronan and its receptors (CD44, RHAMM) regulate the activities of inflammation and cancer, Front. Immunol. 6 (2015). https://doi.org/10.3389/fimmu.2015.00201.
[33] F. Palomba, E. Rampazzo, N. Zaccheroni, M. Malferrari, S. Rapino, V. Greco, C. Satriano, D. Genovese, L. Prodi, Speci fi c, Surface-Driven, and High-A ffi nity Interactions of Fluorescent Hyaluronan with PEGylated Nanomaterials, (2020). https://doi.org/10.1021/acsami.9b17974.

CHAPTER 2-

Fluorogenic Hyaluronan for micro and nano plastics detection and recognition

2.1 Introduction

Plastics are materials based on polymers of synthetic or semi-synthetic origin, which – since their first preparations at the beginning of the last century – have reached a central role in contemporary society in every aspect of human life [1]. Despite the increasing worldwide attention to proper disposal of plastics after their use – either by recycling, converting to energy or landfill – their large majority (ca. 70%) accumulates in the environment [1], where they can persist for a long time. The presence of plastic debris in the environment poses a safety concern to human health owing to direct or indirect effects, and it undoubtedly disturbs ecology – intended as the interrelationships of organisms with their environment and with each other – under many aspects and thus represents a threat also for human supplies and life [2]. The toxicological impacts of microplastics (size

between 5 mm and 1 μm) and of nanoplastics (overall size below 1 μm) are also associated with their sizes, raising considerable concern due to their possible direct interaction with cells. In addition, these smallest fragments are also the most difficult to detect and to eliminate. With decreasing size, plastic particles become more bioavailable to organisms: for example, micro- and nanoplastics (MNPs) have been reported in various taxa across trophic levels, such as plankton, benthic invertebrates, shrimp, bivalves, fish, seabirds [3], [4]. Furthermore, MNPs can be carriers of several kinds of pollutants (heavy metals, plasticizers, etc.) or covered by biofilms, increasing even more their potentially detrimental impacts on the ecosystem. The analysis of MNPs, including the determination of their concentration, chemical nature, size distribution and morphology, remains a goal far to be fulfilled. Several analytical methods have been developed for microparticle analysis, with Fourier transform infrared (FTIR) and Raman spectroscopy representing, at present, the gold standard for microplastic detection and analysis.[5], [6]The analysis of nanoplastics is even more challenging, with protocols still under development. Fluorescence methods – typically endowed with excellent versatility and high sensitivity, low cost and handiness of use

[7] – have found only limited application in the analysis of real samples of MNPs. Fluorescence has been used to trace dye-labelled plastic particles or to recognize plastic debris with fluorescence microscopy after staining them with suitable dyes such as Nile Red.[8]–[13] This dye has been advantageously employed to stain various microplastics in water and also used for high-throughput techniques based on single particle tracking,[14] but its tendency to aggregation causes an increase of the background signal and the occurrence of false-positive features. In addition, its affinity is relatively low towards microplastics, leading to possible desorption and thus posing additional problems.[10]–[12] Very recently, more complex probes based on polyhedral oligomeric silsesquioxane (POSS) derivatized with a coumarin dye were reported and underwent an emission spectral change from yellow to blue upon the interaction with plastic particles of PS, PLA and PMMA in water.[15] Inspired by previous work,[16] in which we observed a strong affinity between RITC-functionalized hyaluronic acid (HA–RB) and PEGylated nanoparticles, in this contribution, we investigate the onset of similar interactions between this long- chain HA functionalized with RB dyes and the surface of different MNPs dispersed in water. Such an interaction

provides a useful fluorescence analytical signal to highlight the presence of MNPs in water due to two overlapping effects. First, HA–RB accumulates on the surface of MNPs driven by a very high affinity, second, the fluorescence quantum yield of the RB moieties increases owing to a hydrophobicity- induced unquenching mechanism, as witnessed by the increase of their average fluorescence lifetime. Finally, the different fluorescence lifetime observed for HA–RB adsorbed on various MNPs and, in particular, on polystyrene MNPs, can provide an absolute parameter to discriminate different types of plastics[17].

2.2 Materials and methods

Lab-grade plastics were either purchased from Sigma Aldrich ("PS", polystyrene 9003-53-6; "PET", poly(ethylene terephthalate) 25038-59-9; "PMMA_ISO", poly(methyl methacrylate)-isotactic 25188-98-1; "PVC", poly(vinyl chloride, 9002-86-2; "PTFE" poly(tetrafluoroethylene) 9002-84-0; "PE", polyethylene 9002-88-4) or obtained by grinding clean and new plastic objects ("PMMA" poly(methyl methacrylate) from a ball mill-grinded disposable fluorescence cuvette). PET and PMMA show

macroscopic/granular fragments and were ground with an analytical mill IKA A10 basic until a fine powder was obtained. The other microplastic samples were already in powder form and were finely ground in a mortar to further reduce mesh size and increase the fraction of nanoplastics and small microplastics.

2.2.1 Scanning electron microscopy

Scanning electron microscopy (SEM) was carried out by using a Philips 515 microscope at an accelerating voltage of 15 kV on the samples fixed with a conducting bi-adhesive tape on an aluminium stub and coated with gold. Images were analysed with ImageJ software.

2.2.2Sample preparation for fluorescence imaging

MNP samples were weighed and incubated under mechanical agitation with 1 mL of water solution containing 170 nM HA– RB. After that, 30 μL volumes of the MNP dispersion were mixed together with a drop of 100 μL hyaluronan hydrogel (16 mg mL−1) directly on the glass slide. This solution volume assures that the hydrogel drop remains viscous during the experiments, to homogeneously disperse the sample and to delay evaporation. The same procedure has

been used to incubate microplastics with Nile Red. In the second set of experiments, we added a purification procedure. Two sets of each microplastic sample were incubated in glass vials under mechanical agitation for 30 min with 1 mL of water solution of 170 nM HA–RB for one set and 5.6 nM HA–RB for the other one. After the incubation, 2 mL of water was added to each vial and then centrifuged at 5000 rpm for 10 min. This process separates MNP fragments, while non-adsorbed HA– RB nanogels remain in the supernatant and 2 mL of it is carefully eliminated with a Pasteur pipette. Then 2 mL of new water was added to each sample and centrifuged again. This washing process was repeated three times. Finally, we mixed the centrifuged MNPs with HA hydrogel for confocal and FLIM imaging.

2.2.3 Photophysical characterization

2.2.3.1 Confocal and FLIM microscopy.

Confocal images were registered on a Nikon A1R microscope with an oil immersion, high NA objective (NA = 1.45, magnification 100×), an excitation laser at 561 nm and a GaAsP PMT with an emission filter at 595/50 nm. The

acquisition parameters were set to 1 A.U., 8× signal average, resonant scanning mode, laser power = 1.64%, PMT GaAsP HV = 70. This setting was kept the same for all the samples analyzed. To obtain large statistic ensembles of MNPs, we acquired 10 × 10 mosaic images, with a final field of view of 1.2 × 1.2 mm2 and a single pixel size of 124 nm. FLIM images were acquired with a time-correlated single photon counting (TCSPC) system (PicoQuant GmbH Berlin), using a 405 nm pulsed excitation laser at a 10 MHz repetition rate, a 560 nm long-pass emission filter, a hybrid PMA detector and a PicoQuant PicoHarp 300 correlation board. FLIM images were then analysed with SymPhoTime 64, PicoQuant GmbH.

2.2.3.2 Image analysis

Confocal images of the different samples have been analysed with a particle tracking macro based on ImageJ commands. The macro was written to process large images with comparable conditions and to obtain relevant information on all the fragments in the area. It processes images to find particles with size greater than the pixel size (124 nm) and pixel intensity higher than a pre-set threshold. The output

includes area, minimum, maximum and mean pixel intensities together with the integral of the identified area.

2.3 Results and discussion

2.3.1 HA–RB synthesis and photophysical characterization

Synthesis of HA–RB was adapted from a previously reported procedure [16]. The HA (200–600 kDa, 30 mg) was dispersed in DMSO (8 mL) and rhodamine B isothiocyanate (RITC, 4.4 mg) was added under stirring; the reaction was left to proceed for 24 h at room temperature. The product was then diluted with water (8 mL) and unreacted RITC was eliminated via dialysis (at least 3 days at room T, regenerated cellulose, cut-off 12 kDa), to finally obtain a dispersion of functionalized HA–RB in water. The probe effective degree of functionalization was evaluated by UV-vis analysis measuring the absorbance of Rhodamine B in ethanol solution at known concentration of HA-RB. Since the two spectra feature similar properties as the free dye we can use with a reasonable assumption the molar extinction coefficient of the free Rhodamine B in ethanol (106000 cm-1M-1). The

HA-RB calculated degree of functionalization is 1.7 % (ca. 1 dye molecule every 60 monomers of hyaluronic acid).[18] Native HA has an intrinsic tendency to form aggregates in water, largely driven by the rigidity of this polyanion;[19] yet, the presence of RB moieties – with their hydrophobic contribution – greatly enhances this tendency and further destabilizes HA–RB polymer chains, leading to the formation of aggregated nanogels in the 100– 300 nm size range.[16] The role of RB dyes in promoting this aggregation in water is proved by the distinctive absorption spectrum of aggregated RB, showing a higher shoulder at 530 nm and a broader peak at 565 nm with respect to the monomeric RB dyes (Figure 2.1†).

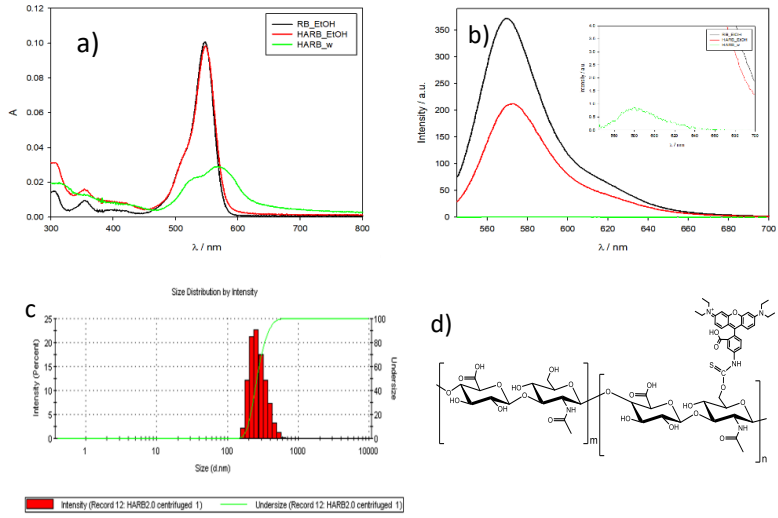

Figure 2.1 *- Absorbance (a) and emission spectra (b, λ_{exc} = 530 nm) of the reference dye Rhodamine B in ethanol (RB_EtOH) and of HA-RB in ethanol and milliQ water solution (HA-RB_EtOH and HA-RB-w, respectively, both at [HA-RB] = 38 nM). Figure c shows the dynamic light scattering measurement of the solution of HA-RB (dH = 320 nm, polydispersity index PdI = 0.287). d) Molecular structure of rhodamine functionalized hyaluronic acid (m/n ~ 60)*

To evaluate the photophysical properties of the HA-RB probe we acquired absorbance and emission for calculation of photoluminescence quantum yield (PLQY). Rhodamine B solution in ethanol was used as a reference (PLQY=0.65). HA-RB spectra were recorded both in ethanol and water

The calculated photoluminescence quantum yield for the probe in the two different solvent is 0.39 for HA-RB in ethanol and 4.2-$\times 10^{-3}$ for HA-RB in Milli-Q water.

The same solutions were used to register the fluorescence lifetime decay with TCSPC experiment (Table 2.1).

Sample	τ (ns)	χ^2
RB (ethanol)	2.9	1.006
HA-RB (ethanol)	2.8	0.903
HA-RB (water)	1.8	1.035

Table 2.1 *- Fluorescence lifetimes of RB dye in ethanol, of HA-RB in ethanol and in water*

RB moieties in the HA–RB nanogels in water suffer from heavy self-quenching, displaying an average PLQY of 0.004 and a lifetime of 1.8 ns, which results in a low fluorescence background for sensing schemes both in a cuvette and in fluorescence microscopy. On the contrary, HA–RB is well soluble in ethanol (whereas native HA is not), and RB moieties here display their typical absorption spectrum and bright emission (PLQY = 0.39).

2.3.2 Fluorescence Mechanism of the probe

Thanks to the properties highlighted with the photophysical characterization, we were able to hypothesize a possible fluorescence mechanism for the probe. That's rely on the intrinsic behaviour of the RB which is well renowned dye that shows self quenching and in a system like our this is the scenario we found: in the probe alone the dye molecules are confined close to each other in hydrophobic pockets and INTER and INTRA-filaments fluorophore close interactions cause the fluorescence self quenching. Instead, When there is a driving force that can guide a progressive uncoiling of the

polymer chain, rhodamine-rhodamine interaction are hindered and we have the enhancement of the fluorescence and the recovery of quantum yield.(Figure. 2.2). The interaction of the probe with silica based nanomaterials has already been investigated [16] and in this work we explore its use in microplastic detection and recognition.

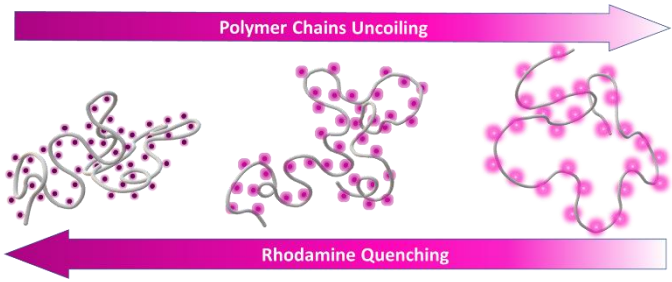

Figure 2.2*-Cartoon representation of the fluorescence enhancement and quantum yield recovery of the hyaluronan based probe.*

2.3.3 HA–RB testing for micro- and nanoplastics

We obtained water-dispersed MNPs from two different sources: for the first sample type, lab-grade microplastics were purchased from Sigma-Aldrich; for the second type, we fragmented intact, non-degraded commercial plastic objects

via ball-milling and/or with a pestle and mortar. Then, each kind of MNP – in the form of a solid powder – was dispersed in distilled water, even though the dispersions were not fully stable since a large part of the MNP fragments was separated either by precipitation or by floating on the water surface. To these heterogeneous dispersions, a small volume of HA–RB in water was added (typically 50 μL to 1 mL of the MNP dispersion), yielding a final HA–RB concentration of ~170 nM (estimated concentration of polymer chains, using 400 kDa as MW). After shaking for 30 seconds, the MNP dispersions were ready for fluorescence microscopy observations, which were performed on a drop of 50 μL of the dispersion deposited on a coverglass. As readily observed by confocal fluorescence microscopy under 561 nm excitation, after mixing with HA–RB, MNPs become brightly luminescent in the 590 ± 30 nm range. Confocal images (Figure 2.3) show that the MNPs are effectively labelled and clearly distinguishable from the background both when the fragments are very large (with a few fragments reaching up to 100 microns in diameter) and when the fragments are about 1 micron in diameter (Figure 2.15-2.17)

Confocal sectioning with oil immersion, high numerical aperture objective (NA = 1.45, magnification 100×) allows

the confirmation that HA–RB labelling is a surface process, and that no penetration of HA–RB in the MNPs occurs, as proven by the dark inner part of the MNPs, which in turn displays a bright fluorescent surface (Figure 2.3)

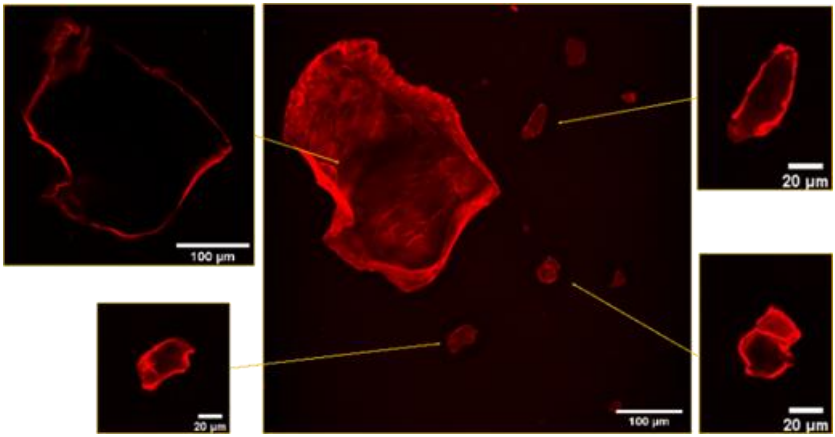

***Figure 2.3**- Confocal fluorescence microscopy of PMMA microparticles in water, in the presence of 170 nM HA–RB. Centre image: an overlap of 55 stacks spanning 66 micrometres in depth. The inset squares show selected individual Z-stacks showing the cross-sections of PMMA microparticles.*

2.3.4 Nile Red + microplastic: false positive for small fragment recognition

Nile Red is a common fluorescent dye for fluorescent staining of microplastics in literature [20], [21]. Samples of microplastic have been incubated in water solution of Nile Red in the same way of HARB probe. The confocal images reveal that Nile Red adsorbs onto microplastics surface leading to fluorescence intensity comparable to MNPs stained with HA-RB. Yet, the images also show the presence of NR aggregates with typical “needle-like” morphology ,from sub-micron to several tens of micrometers, – providing “false positive” fluorescent objects as also previously reported.[22].– that can only be discriminated via FLIM analysis. These NR aggregates can be only distinguished from MNPs only via lifetime imaging analysis, owing to their short lifetime (Figure 2.4†).

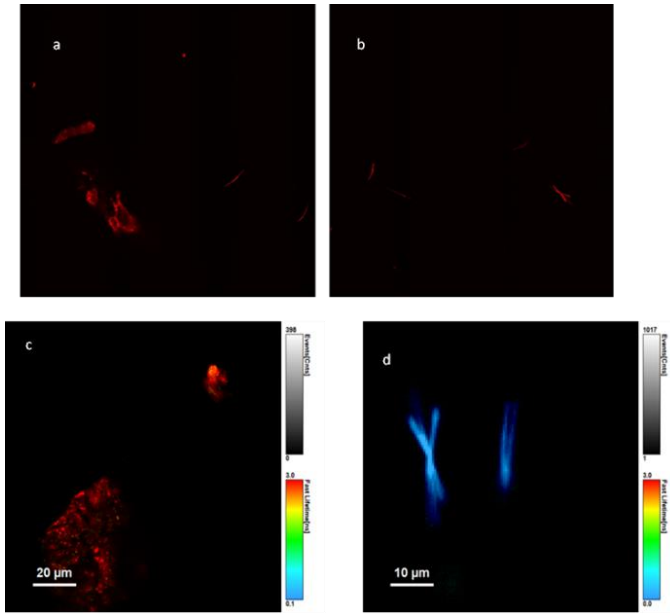

Figure 2.4*- In figures a) and b) are reported two mosaic acquisitions of PMMA+NR where both microplastics fragment and needle-like NR aggregates are present. FLIM images reported in c) and d) show clearly different lifetimes of NR when on PMMA surface respect to its own aggregates.*

2.3.5 Aiming to nanoplastics recognition

Yet, under these conditions and without any purification step, the reference sample of HA–RB in water, in the absence of MNPs, contains small (<500 nm diameter) and poorly

emissive HA–RB aggregates. The presence of nanogels of HA– RB in this size range impedes the unambiguous recognition of nanoplastics of similar size, even if they do not interfere with the identification of microplastics with diameters larger than ca. 1–2 micron. To overcome this issue and allow for clear recognition also of nanoplastics with sizes smaller than 1 micron, we added a centrifugation step (5000 rpm, 10 minutes) that separates MNP fragments, while non-adsorbed HA–RB nanogels – owing to their small size, hydration and density – remain in the supernatant and are eliminated. In the absence of MNPs, with this additional purification step, we could not identify any emissive aggregate (Figure 2.5†).

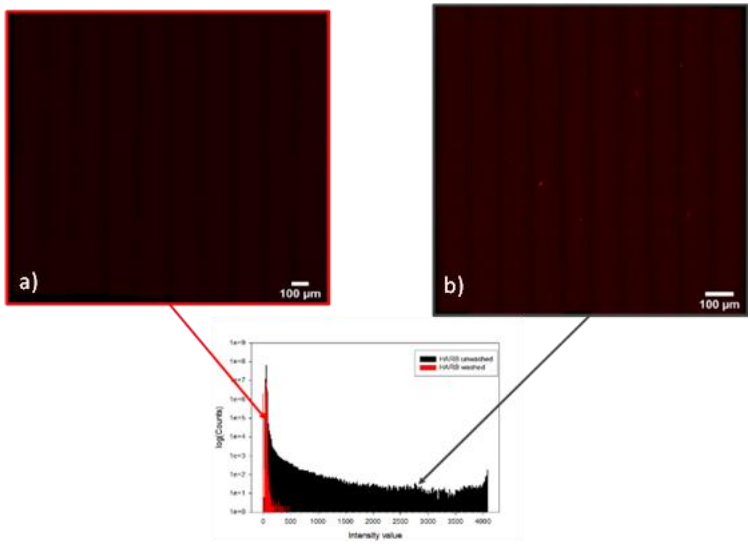

Figure 2.5 - Both the images are a multi-frame 10x10 mosaic acquisition. In a) is reported HA-RB subjected to washing process with 60x magnification objective and in b) HARB which was not processed with 100x magnification. Same acquisition parameters were used and images has been acquired between 30 and 50 micron above the surface

Therefore, sub-micron emissive features in the MNP samples, when treated with this centrifugation step, can also be explicitly attributed to nanoplastics with size as small as the resolution of the microscope (ca. 250 nm). We acquired large images of 5.5 × 5.5 mm^2 (multi-frame mosaic acquisitions of 10 × 10 images at a constant height from the coverglass surface, in the range 5–50 microns from the surface) of the MNP samples labelled with HA–RB (5.6 nM and 170 nM) (Figure 2.6). On the microscope slide, most of the microplastic samples tend to accumulate in a specific region of the drop of the solution they are dispersed in (drop surface and borders). In order to have a homogenous dispersed sample in the drop we used a more viscous medium that does not interfere with the photophysical properties of HA-RB. We tested the probe HA-RB (~ 10^{-5} M) in Glycerol (Gly) and hyaluronan hydrogel (HAgel, 16mg/mL native HA

200-600 KDa in water) monitoring its emission signal at 580 nm through time for the system to equilibrate.

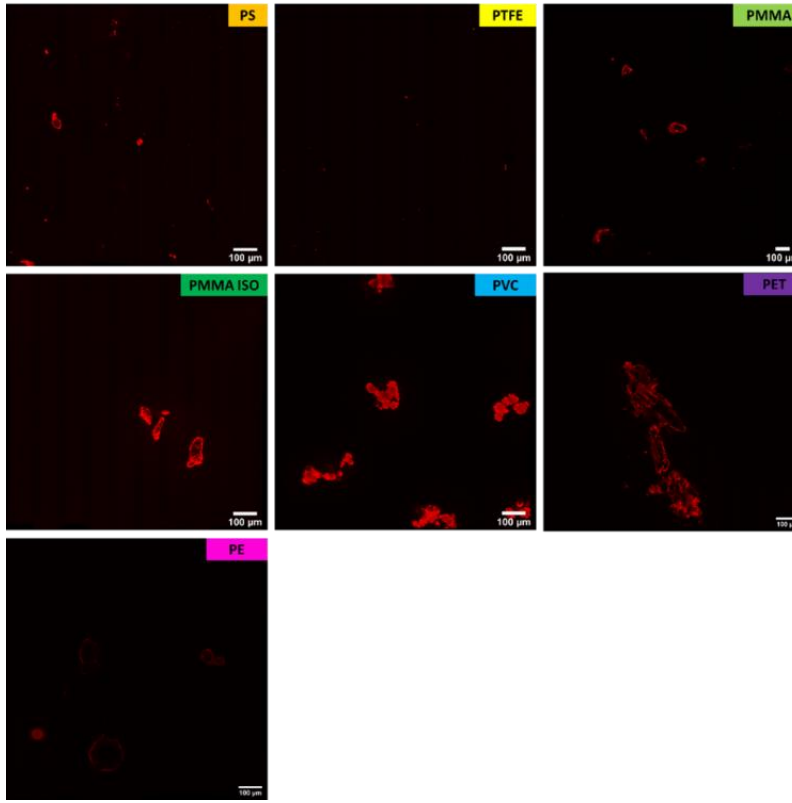

Figure 2.6 *–Confocal images of microplastic samples incubated with 170 nM HA-RB. Acquisition parameters and LUTs are the same for all images*.

As reference we used the emission spectra of Rhodamine B (RB) and HA-RB in Milli-Q water (Figure 2.7).

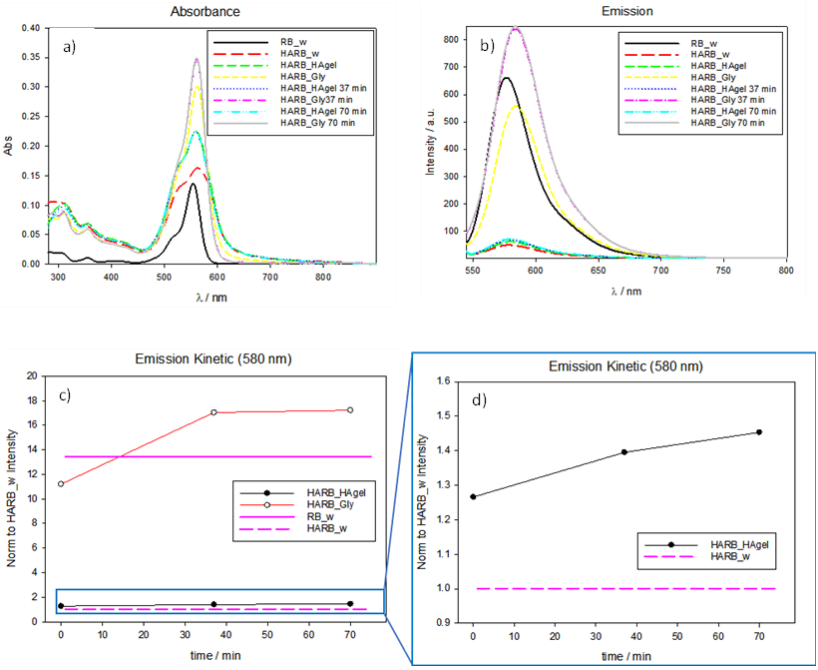

Figure 2.7 *– Absorbance a), emission spectra b) and time-evolution of fluorescence intensity at 580 nm for RB in ethanol, HARB in ethanol and HARB in water c) and d). The fluorescence emission signal was normalized to HA-RB_w value.*

The graph in figure 2.7-b shows that the probe has a significant enhancement of emission in glycerol compared to the native hyaluronan which was selected since it does not

interfere with the photophysical properties of HA-RB. Absorption and emission spectra are slightly red-shifted in glycerol due to solvatochromism. Hence, to best observe the fluorescently stained MNP samples, we immersed them in a hyaluronan hydrogel (16 mg mL^{-1} native HA 200–600 kDa in water) rather than pure water, in order to slow down water evaporation and movement of fragments during acquisition without interfere with the probe photophysical properties. We then analysed the confocal images with a particle tracking routine based on ImageJ, which selects particles based on an intensity threshold value taken well above the background noise (e.g., threshold = ca. 500 counts for background signal = 64 ± 12 counts, detailed description in APPENDIX and Figure 2.14 and 2.15-2.17). Plotting the integrated pixel intensity versus the size (equivalent diameter) of the MNP fragment shows that, as expected, the overall fluorescence signal builds up in the fragments with increasing size (Figure 2.8).

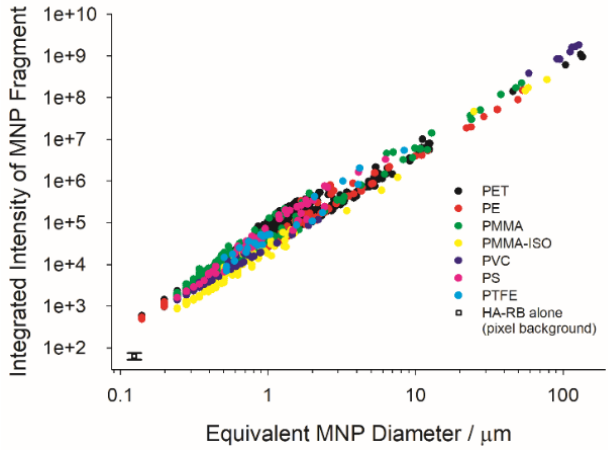

Figure 2.8- Plots of integrated pixel intensity versus the size (equivalent diameter, calculated from the area of the fragments, d =(A/2π)0.5) of the MNP fragment.

The sub-micron part of the plots reveals that a large number of nanoplastics are brightly labelled with HA–RB and that they stand out of the background with an overall intensity which is from ∼10 to >200 times the background noise. In a log–log plot, the intensity shows a clear linear trend, well fitted with a slope close to 2, as expected for a surface adsorption process. The slope, which is slightly larger than 2 for all plastic samples, suggests that microplastics feature rough surfaces with higher fractal dimension.[23] From the fitting, we can calculate the intensity of a nanoplastic fragment of size corresponding to a single pixel (square pixel

of side 124 nm), which allows a ready comparison with the background, showing that MNPs stained with HA–RB display between 3.5 (PMMA-iso) and 7.4 times (PMMA) the average intensity of the background for 124 nm size (Table 2.2).

	INTERCEPT	SLOPE	INTENSITY (LOGI) AT SINGLE PIXEL
PS	4.75	2.43	352 (2.55)
PTFE	4.67	2.25	422 (2.63)
PMMA	4.64	2.17	472 (2.67)
PMMA-iso	4.35	2.19	229 (2.36)
PVC	4.51	2.24	300 (2.48)
PE	4.54	2.12	398 (2.60)
PET	4.64	2.25	416 (2.62)
BACKGROUND	--	--	**64 ± 12 (1.81)**

Table 2.2 *– Fitting parameters of the plot shown in figure 2.8 The log-log datapoints have been fitted with a linear fit, the table reports intercept (i.e., log(I) at diameter = 100 μm), slope and calculated intensity (and log(I)) at single pixel (square of lateral size 124 nm), which is compared with the average background intensity at single pixel*

We compared these results with the use of molecular dye rhodamine B (RB), which is soluble in water. RB shows good affinity towards MNP surfaces, with high luminescence from

the microplastic fragments. Yet, RB is highly emissive also in water, and therefore the high signal from the solution hinders the possibility to detect the small nanoplastic fragments (Figure 2.9).

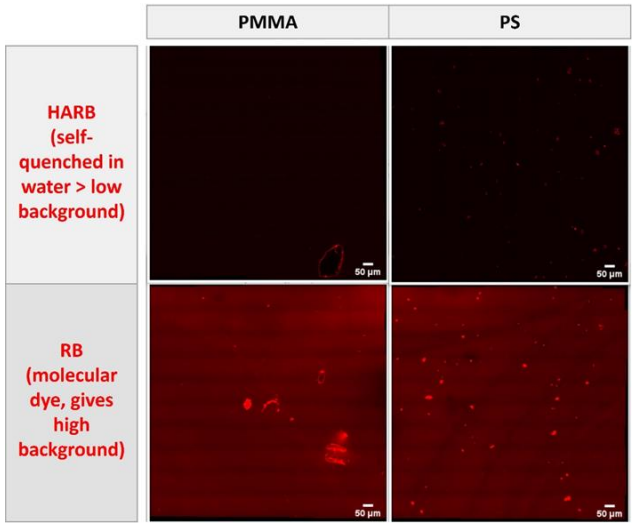

Figure 2.9 *– Comparison of PMMA (left) and PS (right) MNP staining with HA-RB (top) or molecular dye RB (bottom). Larger fragments are still visible with RB molecular dye but the high background does not allow to visualize the smaller nanoplastic fragments.*

2.3.6 Fluorescence lifetime imaging microscopy (FLIM) of MNPs using HA–RB

2.3.6.1 MNP@HA-RB: dependence of lifetime on [HA-RB] concentration

The variation of the excited state lifetime of RB moieties upon interaction with MNPs was also investigated. To evaluate the dependence of lifetime on probe concentration adsorbed on the microplastic surface we incubated 3 samples of PVC with 10 nM, 100 nM and 20 μM HARB (concentration of polymer chains). After the purification steps, the sample was dispersed in the native hyaluronan hydrogel and we acquired confocal and FLIM microscope images with the same optical parameters. As previously found, the lifetime of HA–RB in water is short and multiexponential, corresponding to a broadly self-quenched state. Interestingly, the average lifetime displays relevant variations upon interaction with MNPs, pointing to a conformational change of HA–RB nanogels with a fraction of self-quenched RB moieties becoming emissive from a monomer-like state. In particular, at low concentrations of HA–RB, the fluorescence decay of HA–RB onto MNP

surfaces appears longer and, in some cases, is also more similar to a single- exponential decay with respect to the HA–RB nanogels in water (Figure 2.10).

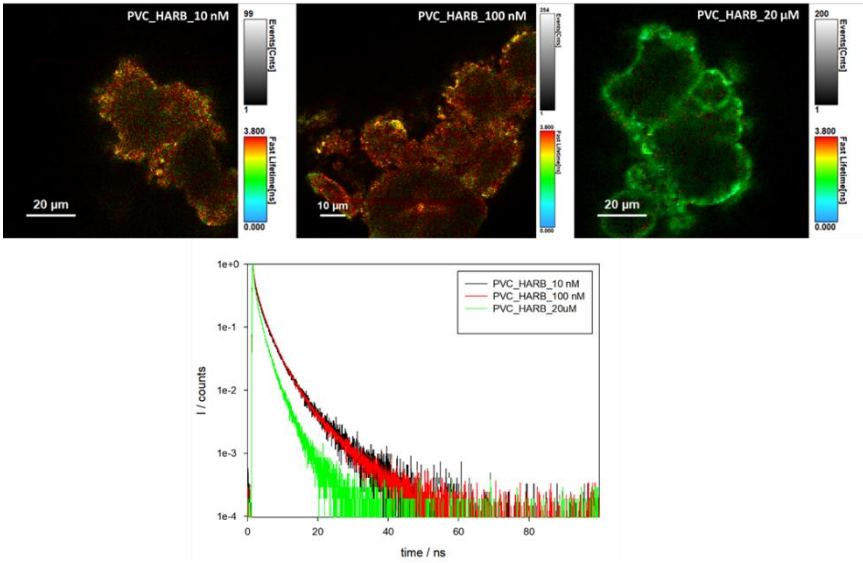

***Figure 2.10**- FLIM acquisitions indicate that 10 nM and 100 nM concentration of the probe lead to the same lifetime decay showing that in this concentration range the photophysical properties of the HA-RB remain unchanged. The higher concentration 20 µM instead show a marked decrease in the lifetime decay due to the accumulation of HA-RB on the microplastic surface favouring the self-quenching of RB moieties*

This can be explained by a hydrophobicity- induced unquenching mechanism: breaking of the RB dimers and aggregates (responsible for the initial self- quenching and for HA–RB aggregation as nanogels) occurs due to conformational changes of HA–RB upon adsorption on the MNP surface, which results in the local increase of the average lifetime, narrowing of the lifetime distribution and, consequently, in the enhancement of the fluorescence quantum yield.

2.3.6.2 MNPs chemical nature recognition through FLIM microscopy

Yet, the conformational changes appear to be quite sensitive to the type of surface, so that an increase of the lifetime of different magnitude is observed for different types of MNPs.

Therefore, it is noteworthy to underline that, under these conditions, the chemical nature of MNPs can be made evident via FLIM analysis, allowing for a straightforward distinction as shown in Figure 2.11 for PS and PMMA microplastics, which can be clearly recognized even when mixed.

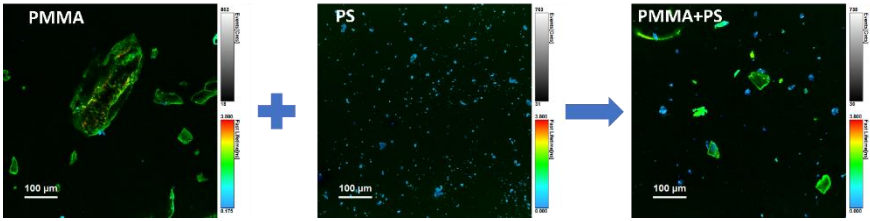

Figure 2.11 *FLIM microscopy images of PMMA and PS MNPs labelled with HA–RB, before and after mixing (20x magnification).*

The lifetime dependence on the specific plastic surface could be explained by the interplay of two different interactions: the first is the hydrophobic interaction, which causes the increase of lifetime, and which characterizes the binding of HA–RB onto the surfaces of purely hydrophobic plastics such as PTFE and PVC. The second interaction that can play a role in the affinity with MNP surfaces is the H-bond formation due to the hyaluronan functional groups of HA–RB, which may be more relevant in the binding with less hydrophobic surfaces of PMMA and PET MNPs. Compared to the other plastic polymers, PS shows a peculiar behaviour, in which electronic interactions with the styrene units may be at the basis of the short and approximately monoexponential lifetime of HA–RB. Yet, the build-up of HA–RB layers on MNP surfaces, at higher HA–RB concentrations, changes

again the photophysics of the RB moieties. The local intensity on the surface of MNPs increases, but the emission decay gradually becomes shorter and multiexponential. The additional HA– RB on the surface of MNPs indeed increases the local density of RB dyes and therefore the probability of self-quenching interactions among RB moieties is enhanced, resulting in the observed shorter and multiexponential lifetime (Figure 2.12).

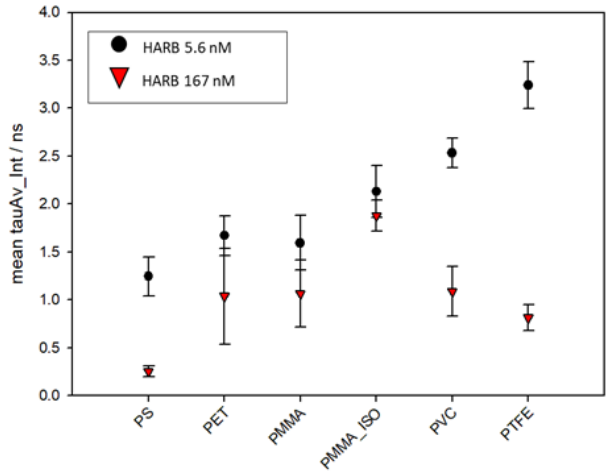

***Figure 2.12**-Mean values with standard deviations of "τ_Av_Int", i.e., the average lifetime weighted on intensity, for MNP*

For these reasons, a low concentration of HA–RB should be used for discriminating among the different kinds of plastics;

this concentration is, however, highly sufficient to give a clear image (Figure 2.11 and 2.13).

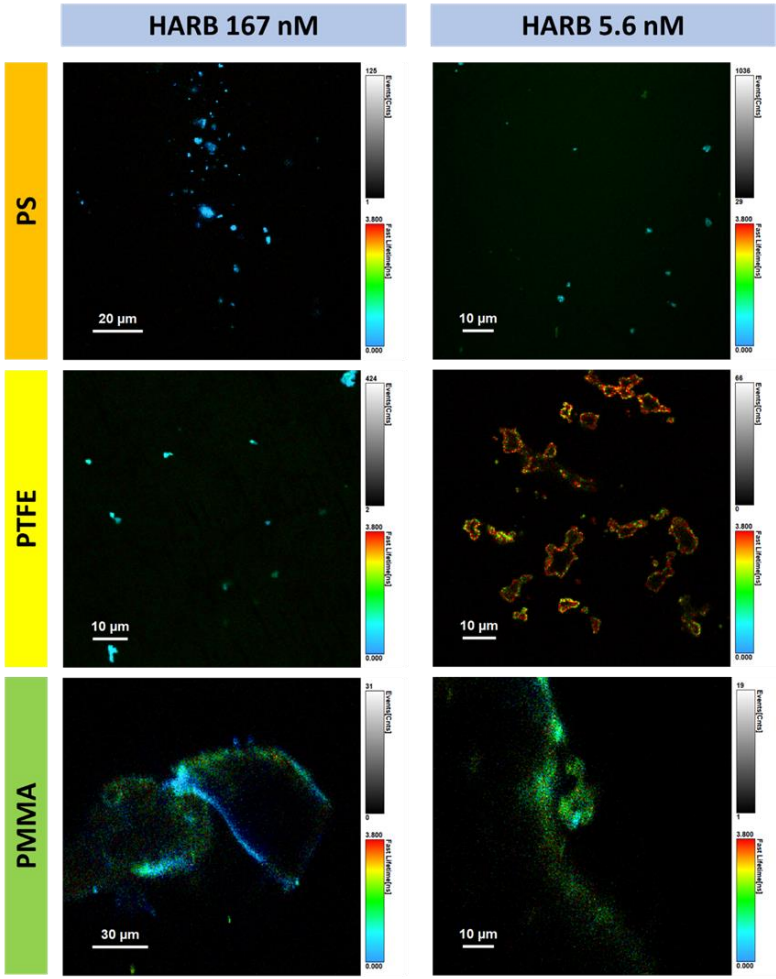

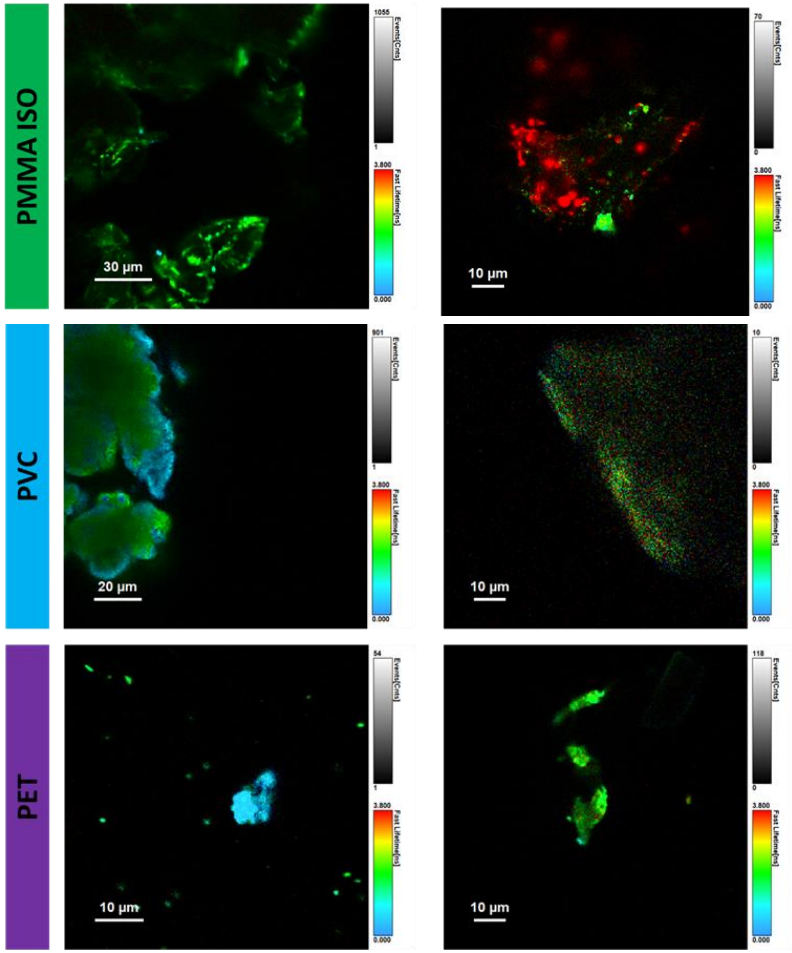

.

***Figure 2.13**- FLIM images of MNPs sample at two concentrations of HA-RB (left images [HA-RB] = 167 nM, right images [HA-RB] = 5.6 nM.*

The ability of HA–RB to readily stain micro- and nanoplastics even at extremely low concentration (∼5 nM polymer chain and ∼100 nM rhodamine B dyes, to be compared with the typical concentration used for the tests based on Nile Red, in the range 1–10 μM) can be explained by the concomitant effect of a high affinity of the HA–RB nanoprobe towards many plastic surfaces and by high PLQY due to the effective switch-ON of the luminescence of RB moieties upon adhesion of the probe onto these surfaces.

2.4 Conclusions

In conclusion, we report here a fluorogenic material, i.e., hyaluronic acid functionalized with rhodamine B (HA–RB), with a very weak fluorescence intensity in water, but readily adsorbs onto the surface of various MNPs with a concomitant enhancement of brightness, making them fluorescent. Fluorescently stained MNPs are clearly visible with size as small as the resolution of a confocal microscope, with nanoplastic fragments of approximately 250 nm standing out of the background. This high sensitivity can be achieved due to the recovery of the fluorescence quantum yield of the RB moieties thanks to a hydrophobicity-induced unquenching mechanism together with a high affinity interaction with MNPs. These properties allow for MNP detection even at a very low concentration of the probe (~5 nM). Furthermore, the lifetime parameter reveals a different degree of hydrophobicity-induced unquenching of HA–RB on the surface of different microplastics, making possible the identification of the types of MNPs based on their fluorescence lifetime. These results represent a feasibility study, under controlled conditions, and its applicability to real MNP debris in environmental samples remains a challenge. The intrinsic versatility of the reported fluorogenic

hyaluronan, though, represents a valuable strength: in fact, various properties of fluorogenic hyaluronan nanogels can be finely tuned by changing the mass, the derivatization or even the chemistry of HA and of the fluorogenic moiety. This dimension range is quite below the detection limit of already established techniques employed in this research field such as micro-FTIR spectroscopy (~50 μm detection limit) and micro-Raman (~5 μm detection limit). This versatility is potentially very advantageous to design custom probes for different applications, in which sensitivity requires proper balance with selectivity towards various categories of interferents and with different experimental conditions.

2.5 APPENDIX -Image analysis

2.5.1 FLIM

FLIM images were analysed with SymPhoTime 64, PicoQuant GmbH. For each image we selected different regions of interest (ROIs) relative to the microplastic surface and each associated lifetime decay was fitted with "n-Exponential Reconvolution Fit" model. In all cases we use either 2 or 3 exponentials to obtain satisfactory fittings, probably due to the heterogeneous nature of the RB dyes in the HA-RB nanogels and on the non- homogeneous unquenching upon interaction with MNPs surfaces. Therefore, for each sample, we took the τ_Av_Int of the ROIs as the parameter to compare different decays, and we calculated the mean value and the associated standard deviation to statistically compare the lifetime decay of different microplastics (resulting in the dataset plotted in figure 2.12).

2.5.2 Confocal Images: Size vs Intensity Analysis

The confocal images have been analysed with an ImageJ based macro that finds particles with free shape, size larger than the optical resolution of the microscope, and pixel intensity above a certain threshold. The intensity threshold can be set visually to check that no background pixels are included in the analysis. The results output includes area, minimum, maximum, mean pixel intensities and Intensity integral of the area identified. The threshold value is established on a sample of 170 nM HA-RB subjected to washing process in hyaluronan hydrogel used as reference (Figure 2.5). This sample ensures the absence of HA-RB aggregates. From the logarithmic intensity histogram, we chose the intensity threshold to ca. 500 counts, well above background noise (64 ± 12 counts) and slightly varies when we set it for the analysis of different samples. Also, the macro is written to recognize objects above a single pixel size (124 nm) among the selected free shape above the intensity threshold value. These two criteria together with the resolution limit of the instrument (250 nm) show that the analysis result can recognize sub-micron fragment in the

MNPs sample (Figure 2.14). In figure 2.14 we report the workflow of MNPs image acquisition and analysis.

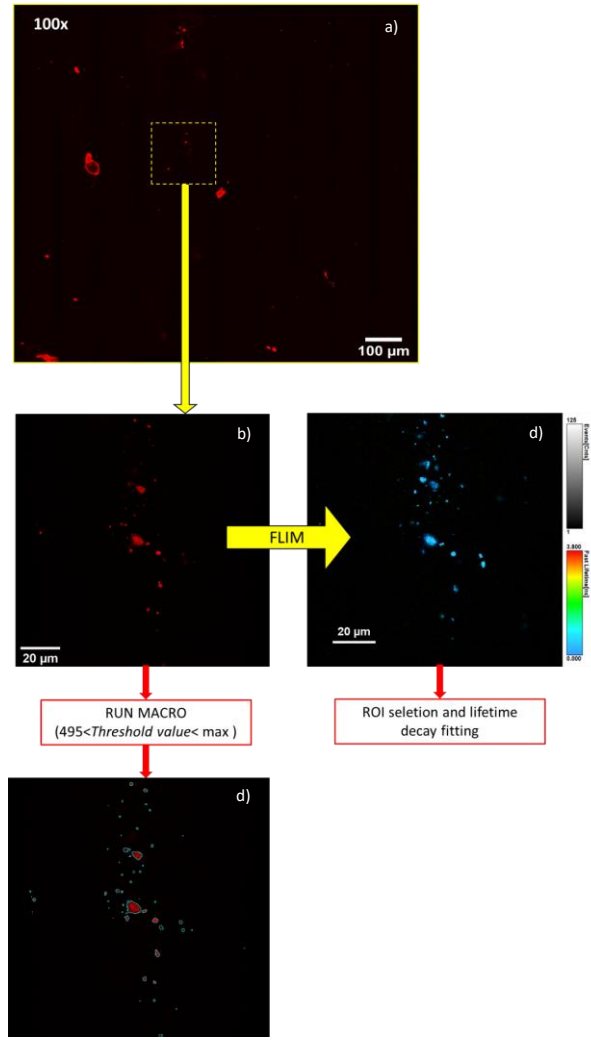

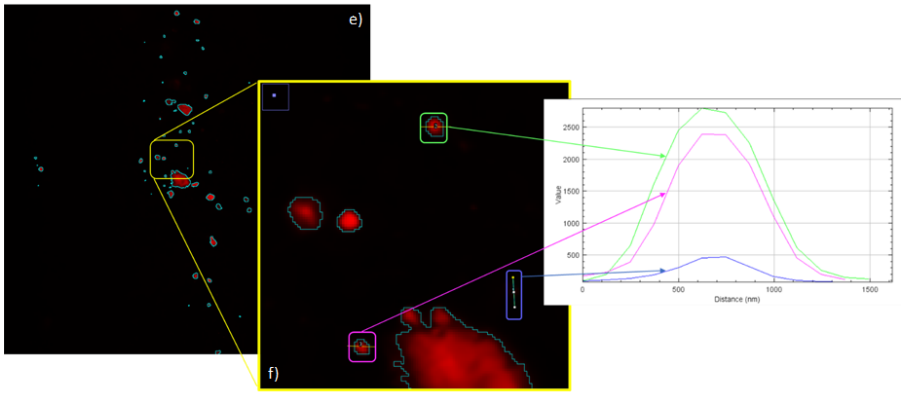

Figure 2.14 *- Workflow of the acquisition and analysis process for PS microplastic sample. The image a shows a e) 10x10 mosaic acquisitions with 100x magnification; image b is a single capture and c its corresponding FLIM image; image d shows the resulting area identified by the macro. In the image f there is an enlargement of small fragments identified by the macro routine which intensity profiles (green and pink curve) demonstrate the ability of sub-micron plastics recognition (ca. 500 nm FWHM). The blue curve is associated to a really small fragment whose intensity is equal to the lower value of the threshold and whose dimension is comparable to the microscope resolution limit.*

2.5.3 SEM images of representative MNPs

The SEM micrographs of some representative MNPs samples clearly show, despite the sticking interactions, the presence of fragments of size both above and below one micron.,

These results confirm the wide size distribution of our samples, already observed by confocal microscopy.

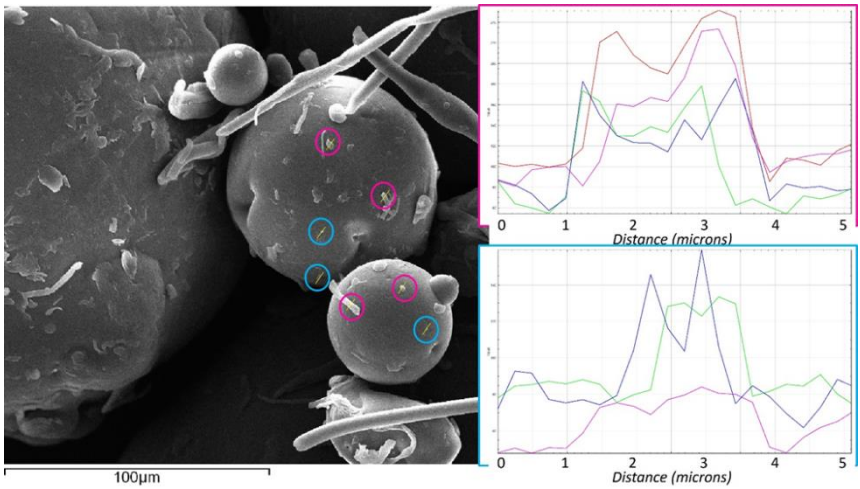

Figure 2.15 *– SEM micrograph of PE MNPs*

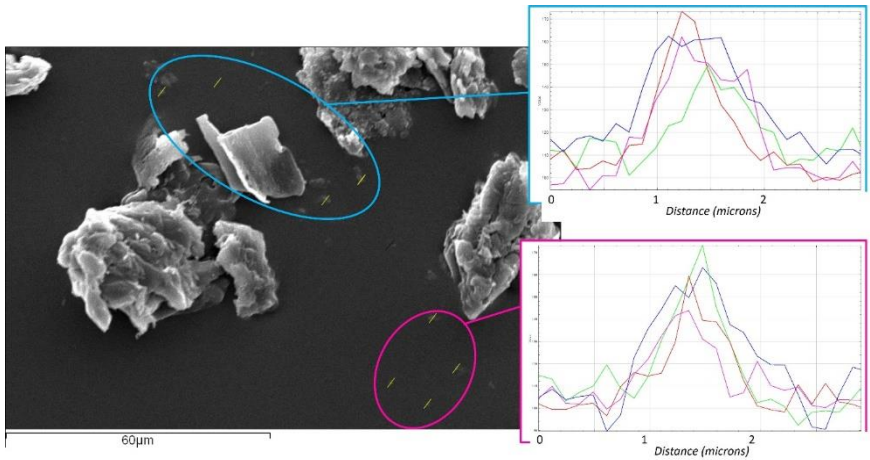

Figure 2.16 *– SEM micrograph of PMMA MNPs.*

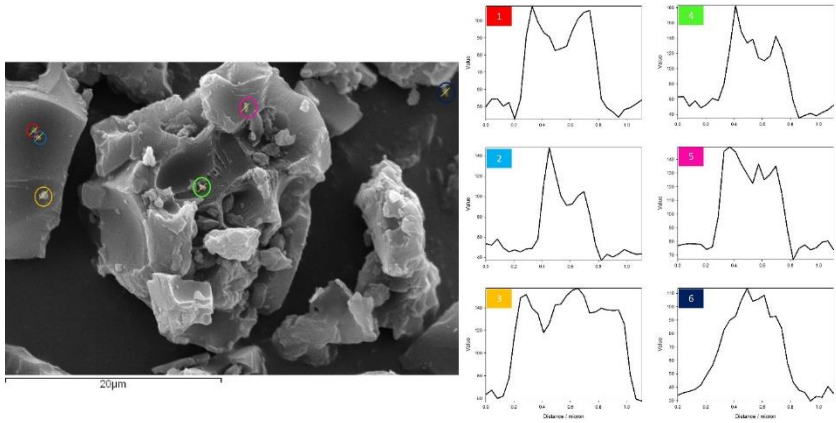

Figure 2.17 *– SEM micrograph of PS MNPs.*

2.6 References

[1] M. Enfrin, L. F. Dumée, and J. Lee, "Nano/microplastics in water and wastewater treatment processes – Origin, impact and potential solutions," *Water Research*, vol. 161. pp. 621–638, 2019.

[2] A. Ragusa *et al.*, "Plasticenta: First evidence of microplastics in human placenta," *Environ. Int.*, vol. 146, p. 106274, 2021.

[3] W. J. Shim, S. H. Hong, and S. E. Eo, "Identification methods in microplastic analysis: A review," *Analytical Methods*, vol. 9, no. 9. The Royal Society of Chemistry, pp. 1384–1391, 2017.

[4] "https://ec.europa.eu/environment/marine/good-environmental-status/descriptor-10/pdf/GESAMP_microplastics%20full%20study.pdf." .

[5] A. Käppler *et al.*, "Analysis of environmental microplastics by vibrational microspectroscopy: FTIR, Raman or both?," *Anal. Bioanal. Chem.*,

vol. 408, no. 29, pp. 8377–8391, 2016.

[6] C. Fang *et al.*, “Identification and visualisation of microplastics / nanoplastics by Raman imaging (iii): algorithm to cross-check multi-images,” *Water Res.*, vol. 194, p. 116913, 2021.

[7] A. Credi and L. Prodi, “From observed to corrected luminescence intensity of solution systems : an easy-to-apply correction method for standard spectrofluorimeters,” *Spectrochim. Acta Part A Mol. Biomol. Spectrosc.*, vol. 54, pp. 159–170, 1998.

[8] J. C. Prata, V. Reis, J. T. V. Matos, J. P. da Costa, A. C. Duarte, and T. Rocha-Santos, “A new approach for routine quantification of microplastics using Nile Red and automated software (MP-VAT),” *Sci. Total Environ.*, vol. 690, pp. 1277–1283, 2019.

[9] L. Lv *et al.*, “A simple method for detecting and quantifying microplastics utilizing fluorescent dyes - Safranine T, fluorescein isophosphate, Nile red based on thermal expansion and contraction

property," *Environ. Pollut.*, vol. 255, p. 113283, 2019.

[10] G. Erni-Cassola, M. I. Gibson, R. C. Thompson, and J. A. Christie-Oleza, "Lost, but Found with Nile Red: A Novel Method for Detecting and Quantifying Small Microplastics (1 mm to 20 μm) in Environmental Samples," *Environ. Sci. Technol.*, vol. 51, no. 23, pp. 13641–13648, Dec. 2017.

[11] T. Maes, R. Jessop, N. Wellner, K. Haupt, and A. G. Mayes, "A rapid-screening approach to detect and quantify microplastics based on fluorescent tagging with Nile Red," *Sci. Rep.*, vol. 7, no. 1, p. 44501, 2017.

[12] W. J. Shim, Y. K. Song, S. H. Hong, and M. Jang, "Identification and quantification of microplastics using Nile Red staining," *Mar. Pollut. Bull.*, vol. 113, no. 1–2, pp. 469–476, 2016.

[13] A. I. Catarino, A. Frutos, and T. B. Henry, "Use of fluorescent-labelled nanoplastics (NPs) to demonstrate NP absorption is inconclusive without

adequate controls," *Sci. Total Environ.*, vol. 670, pp. 915–920, 2019.

[14] R. Molenaar, S. Chatterjee, B. Kamphuis, I. M. J. Segers-Nolten, M. M. A. E. Claessens, and C. Blum, "Nanoplastic sizes and numbers: quantification by single particle tracking," *Environ. Sci. Nano*, vol. 8, no. 3, pp. 723–730, 2021.

[15] R. Nakamura, H. Narikiyo, M. Gon, K. Tanaka, and Y. Chujo, "An optical sensor for discriminating the chemical compositions and sizes of plastic particles in water based on water-soluble networks consisting of polyhedral oligomeric silsesquioxane presenting dual-color luminescence," *Mater. Chem. Front.*, vol. 3, no. 12, pp. 2690–2695, 2019.

[16] F. Palomba *et al.*, "Specific, Surface-Driven, and High-Affinity Interactions of Fluorescent Hyaluronan with PEGylated Nanomaterials," *ACS Appl. Mater. Interfaces*, vol. 12, no. 6, pp. 6806–6813, 2020.

[17] M. Cingolani, E. RAMPAZZO, N. Zaccheroni, D. Genovese, and L. Prodi, “Fluorogenic hyaluronan nanogels for detection of micro- and nanoplastics in water,” *Environ. Sci. Nano*, 2022.

[18] J. M. Dixon, M. Taniguchi, and J. S. Lindsey, “PhotochemCAD 2: A Refined Program with Accompanying Spectral Databases for Photochemical Calculations¶,” *Photochem. Photobiol.*, vol. 81, no. 1, p. 212, 2005.

[19] C. E. Reed, X. Li, and W. F. Reed, “The effects of pH on hyaluronate as observed by light scattering,” *Biopolymers*, vol. 28, no. 11, pp. 1981–2000, Nov. 1989.

[20] E. Hengstmann and E. K. Fischer, “Nile red staining in microplastic analysis — proposal for a reliable and fast identification approach for large microplastics,” 2019.

[21] N. Meyers *et al.*, “Science of the Total Environment Microplastic detection and identi fi cation by Nile red staining : Towards a semi-automated , cost- and time-effective technique,”

Sci. Total Environ., vol. 823, p. 153441, 2022.

[22] T. Stanton, M. Johnson, P. Nathanail, R. L. Gomes, T. Needham, and A. Burson, “Exploring the E ffi cacy of Nile Red in Microplastic Quanti fi cation : A Costaining Approach,” 2019.

[23] C. A. Brown, W. A. Johnsen, R. M. Butland, and J. Bryan, “Scale-Sensitive Fractal Analysis of Turned Surfaces,” *CIRP Ann.*, vol. 45, no. 1, pp. 515–518, 1996.

CHAPTER 3-

Protein aggregation kinetic: fluorescent hyaluronan probe for early-stage aggregates detection

3.1 Introduction

Proteins are among the most abundant organic molecules based on 20 fundamentals L-amino acids having different charge, lipophilicity, H-bond capability, and possibility for different other specific interactions such as disulphide bonds and metal coordination. Moreover, to fulfil their task in the complex biochemical reactions in biological processes, each protein presents its peculiar conformation (native structure) and this folding is generally thermodynamically favoured. Nevertheless, this equilibrium can be altered towards other possible conformations in a reversible or irreversible manner, in some cases associated with a toxic effect for the cells which could be the starting point of a disease.[1] More specifically, the difference in energy with different conformations could be very subtle and the energy barrier may be overcome due to many physico-chemical

transformations involving pH, temperature, oxidative stress, crowding effects or interaction with other biomolecules such as glycosaminoglycan (GAGs) [2-4]. When the native conformation is altered or drastically changed, the protein will expose different amino acid residues lowering its colloidal stability with a tendency to aggregation and/or phase separation. The disruption of the appropriate folding of a protein and the subsequent abnormal aggregation is broadly reported in literature as an occurring phenomenon strictly related to the incidence of severe human diseases, specifically to neurological disorders (e.g. Alzheimer's disease (AD), Parkinson's disease (PD), Huntington's disease (HD), amyotrophic lateral sclerosis (ALS) and prion diseases) [5] and type II diabetes.[6] Protein aggregation has been also observed in different model organisms including bacteria (e.g. Eschirichia coli[7]), yeast[8,9], nematodes (e.g. Caenorhabditis elegans)[10,11] and plant cell cultures[12,13] as a consequence of stress conditions such as ageing and heat stress. In this context, the development of methods for a deep comprehension of the molecular pathways of protein aggregation is vital especially for the early-stage processes in protein aggregation and the detection of pathological hallmarks for an effective understanding and tackling of these

diseases. Techniques exploiting luminescence showed their powerful potential to efficiently monitor the presence or the growth of protein aggregates. In particular, the molecular rotor Thioflavin-T (ThT) has proven to be selective towards the presence of beta sheets as in amyloid fibrillar aggregates;[14] other molecular fluorophores such as Congo Red and Nile Red allowed monitoring of non-beta sheet aggregates, even if with lower sensitivity. Recently, other molecular dyes emitting in the NIR range were developed for in-depth *in-vivo* imaging and for super resolution imaging.[15–17] Despite the success of monitoring protein aggregation with fluorescent molecular sensors, it is quite difficult to merge in a single dye many sought properties such as sensitivity, selectivity, targeting, suitable excitation and emission spectral range, and suitability for in vivo diagnostics (i.e., biocompatibility, solubility, ability to pass the blood–brain–barrier, BBB). More recently, the field of luminescent sensors for protein aggregation has been enriched with a variety of novel tools based on nanostructured probes – featuring multiple compartments and functionalities [18] – aggregation-induced-emission fluorogenic compounds (AIEgens),[19] and macromolecules

such as luminescent conjugated oligomers and polymers (LCO and LCP) [20].

Here we report the study of the interaction between a natural biopolymer, the hyaluronan, functionalized with rhodamine B (HA-RB), and the GAPDH metabolic enzyme of *Arabidopsis thaliana*, i.e., GAPC1, that we choose as a case study. The aggregation of GAPC1 in response to controlled oxidative stress has been recently characterized. In particular, it has been highlighted that S-glutationilation driven by oxidation can reversibly inactivates GAPC1 protecting the enzyme and preventing irreversible oxidation. As long as the glutathionylated AtGAPC1 can be deglutathionylised by cytoplasmic oxidoreductases (thioredoxin, glutaredoxin)[21], the temporary inactivation fits into the metabolic remodeling of aerobic cells under oxidative stress conditions.

3.2 Materials and methods

3.2.1 Sample preparation for aggregation kinetic experiment

The solution for aggregation experiment was prepared adding to a buffer solution of TRIS-EDTA (pH = 7,4; filtered with a RC filter 0.2 nm) these reagents in the following order: HA-RB (100 nM); NADH (0.14 mM); GSH (0.625 mM); H2O2 (0.125 mM); GAPC1 (5 mM). In the experiments involving the tuning of the lag-phase it has also been added to the solution NaCl at a concentration of 200 mM. All the reagents except the HA-RB probe, the purification of the GAPC1 and the activity test of the protein were provided and done by the group of Prof. Mirko Zaffagnini (Department of Pharmacy and Biotechnology, University of Bologna).

3.2.2 Laser-sheet microscopy setup for nanoparticle tracking analysis (NTA)

Theoretical base of the technique can be found in the appendix A.8 section.The optical setup has been put together using a Melles Griot 43 ion tuneable laser (model 35 lap) as excitation source (λ_{exc}= 514 nm) and two plano-convex cylindrical lenses (CL #1 focus distance is 200 mm and CL#2

is 50 mm) as beam shapers in order to have a thin laser-sheet in the optical path of the detector. In the optical path of the detector we put a Olympus UPlanFL N 10x Microscope Objective collecting the signal from the sample holder, an emission filter (550 nm) and as a detector we used a electron amplified camera PhotonMAX:512B that can reach single molecule sensitivity (Figure 3.1)

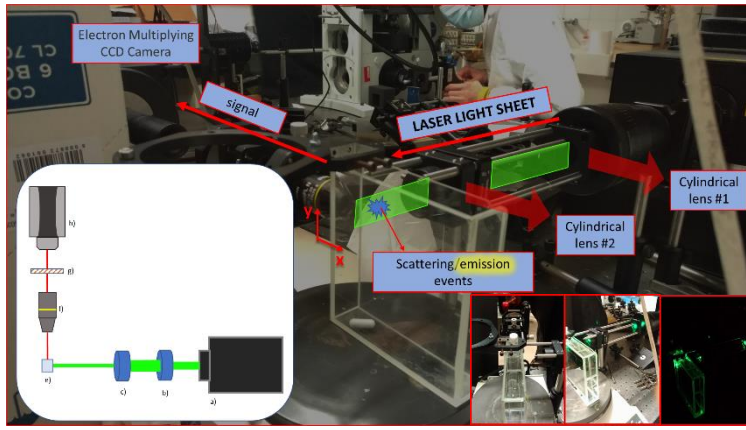

Fig. 3.1*- Picture of the optical setup and inset with the simplified scheme: a) laser source; b) cylindrical lens 1; c) cylindrical lens 2; d) cuvette location; e) objective; f) emission filter; g) detection camera.*

All the acquisitions have been performed in *Non-Overlap Mode* with 35 msec exposure time and acquiring 1000 frames (calculated frame per second FPS= 14) (Figure 3.2).

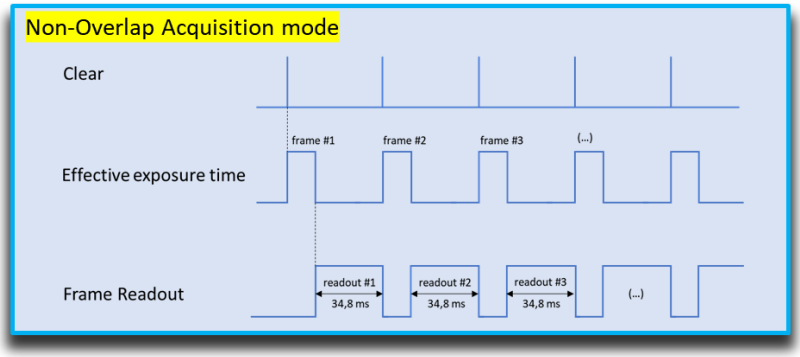

Fig. 3.2*- Scheme of the acquisition mode of the CCD. In the non-overlap mode the FPS can be calculated with* $FPS=1/T_n=1/(t_{exp}*N)+(t_R*N)$ *where N is the number of frames;* t_R *is the readout time for one frame;* t_{exp} *is the exposure time and* T_n *is the total time took to capture a sequence of N frames.*

Calibration of the images has been performed acquiring a picture of a PELCO FORMVAR 400 mesh (Figure 3.3).

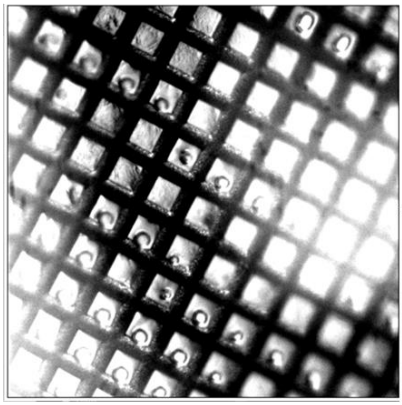

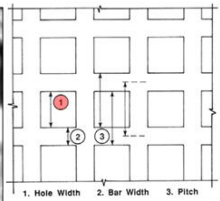

PELCO® Grids

Square Mesh	Pitch µm	Hole µm	Bar µm	% Transmis-sion
50	508	425	83	70
75	339	284	55	70
100	254	204	50	65
150	169	125	44	60
200	127	90	37	50
300	85	54	31	40
400	64	38	26	35

Fig. 3.3- *Acquisition of the formvar grid. Calibration has been performed measuring 10 holes and dividing it by the pitch value. In this way the calculated pixel size is 1.52 µm.*

3.3 Results and discussion

3.3.1 GAPC1

Colloidal stability of proteins in solution can be monitored with light scattering methods, using DLS or even turbidity measurements. These techniques showed that native GAPC1 in solution (0.2 mg/mL) is stable for hours at room temperature, and that H_2O_2 (125 µM) at a 25:1 ratio with

GAPC1 subunits inactivates the protein functionality, whereas GSH together with H_2O_2 (5:1 ratio) caused dramatic protein aggregation.[21] In this previous publication it was underlined that the increase in turbidity followed a lag phase of 15 to 20 min and proceeded for more than 1 h, reaching a plateau in about 2 h (Fig. 1A). The initial hydrodynamic diameter (d_H) of 9.2 ± 0.5 nm was calculated for soluble GAPC1, a value compatible with the crystal structure of GAPC1 tetramers,[22] while aggregates formed after 90 min incubation with H_2O_2 and GSH exhibited irregular shapes resulting from the random binding of nearly globular particles of ~ 300 to 500 nm, with no formation of fibrils. GAPC1 could thus stay glutathionylated for about 10 min without changing significantly its overall native conformation. In this "pre-aggregation phase", enzyme activity can be fully recovered. True aggregation starts only later, during the "oligomeric phase". In this phase, recover of GAPC1 activity becomes less and less efficient, indicating that oligomerization is associated with a permanently inactivated state of the protein. At the end of the lag phase (ca. 20 minutes), GAPC1 aggregates are still rather small (d_H < 100 nm) and are only barely visible with light scattering techniques. In the third phase particles abruptly start to grow

to reach sub- micrometric dimensions. Final aggregates are made by hundreds of bead-like particles of roughly 500 nm in d_H, linked together to form irregularly branched chains. In this work we focus on the "oligomeric phase" of the redox-triggered aggregation of GAPC1 protein, which is elusive to light scattering based techniques, and which could not be studied with fluorescence-based techniques using ThT or Congo Red as fluorescent probes.

3.3.2 HA-RB interaction with GAPC1

In our study, we proceeded by monitoring the aggregation process of GAPC1 in the presence of HA-RB as fluorescent probe simultaneously with luminescence spectroscopy and DLS. Triplicate measurements show a reproducible trend in which fluorescence starts to grow only a few minutes after the beginning of the aggregation kinetics, while DLS confirms that pronounced scattering enhancement takes place only after the lag-phase of 15-20 min.

3.3.3 Cuvette Fluorescence Essay

We started with testing the interaction of the HA-RB with the GAPC1. The experiment consists in preparing a 2 mL

aggregation solution and split it in two 1 mL cuvettes to follow the fluorescence signal at the spectrofluorometer and the scattering signal at the DLS. Both signals have been monitored for 100 minutes when the aggregation kinetic reaches its plateau. The observed fluorescence enhancement can be explained with the partial unquenching driven by hydrophobic interactions between HA-RB and the misfolded GAPC1 protein, which progressively expose hydrophobic residues on their surface responsible also for the aggregation process. The overall enhancement reaches a plateau at ~2 times the starting value, yet the peculiar enhancement during the lag-phase bears potential for further investigations (Figure 3.4).

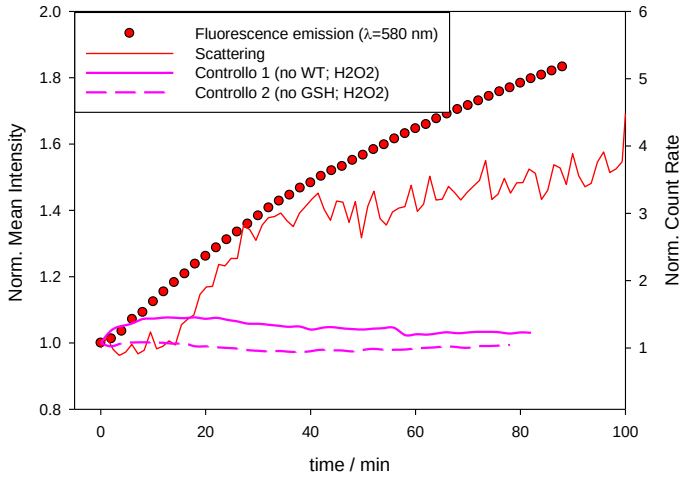

Fig. 3.4 *– In the graph are reported the fluorescence signal, scattering signal from DLS, and fluorescence control experiments for the protein aggregation kinetic of HA-RB GAPC1 (λ_{exc}=530 nm).*

We also made a comparison experiment using Thioflavin T (ThT) that can be taken, as discussed above, as a model probe for investigating protein aggregation.

The fluorescence signal of ThT, differently from that of HA-RB, shows a lag-phase of 20 minutes, similar to the one detected via scattering-based methods (Figure 3.5).

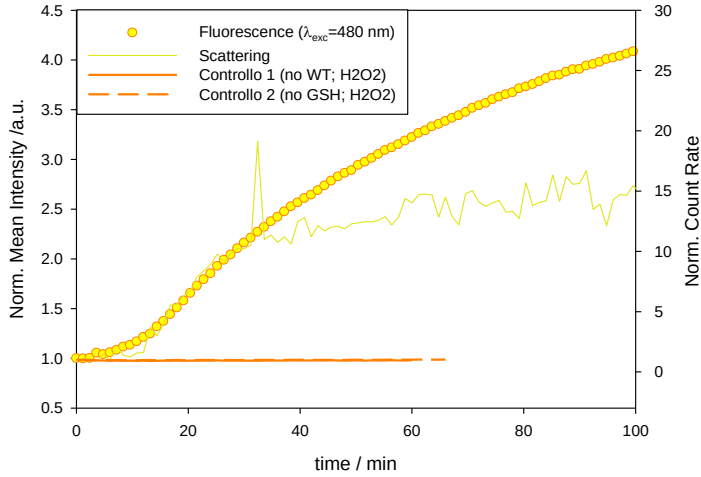

Fig. 3.5 *– In the graph are reported the fluorescence signal, scattering signal from DLS, and fluorescence control experiments for the protein aggregation kinetic of ThT GAPC1 (λ_{exc}=430 nm).*

In living cells, all the homeostatic mechanisms happen in presence of an high concentration of ions in the mM region playing a fundamental role in all the biochemical processes. In this perspective we wanted to reproduce an environment with high ionic strength with NaCl to get closer to the real situation where we can find the protein. Interestingly, together with our collaborator, we found out that the concentration of NaCl is an easy handle to tune the duration of the lag phase, with an increase of the lag time increasing NaCl concentration without affecting the protein activity. Based on this finding, we decided to investigate the initial steps of the aggregation kinetics in presence of 200 mM NaCl, with the aim of prolonging the lag-phase and to gain more detail on the pre-aggregation events. We then repeated the fluorescence assays with HA-RB and ThT in presence of NaCl, simultaneously with DLS monitoring. (Figure 3.6).

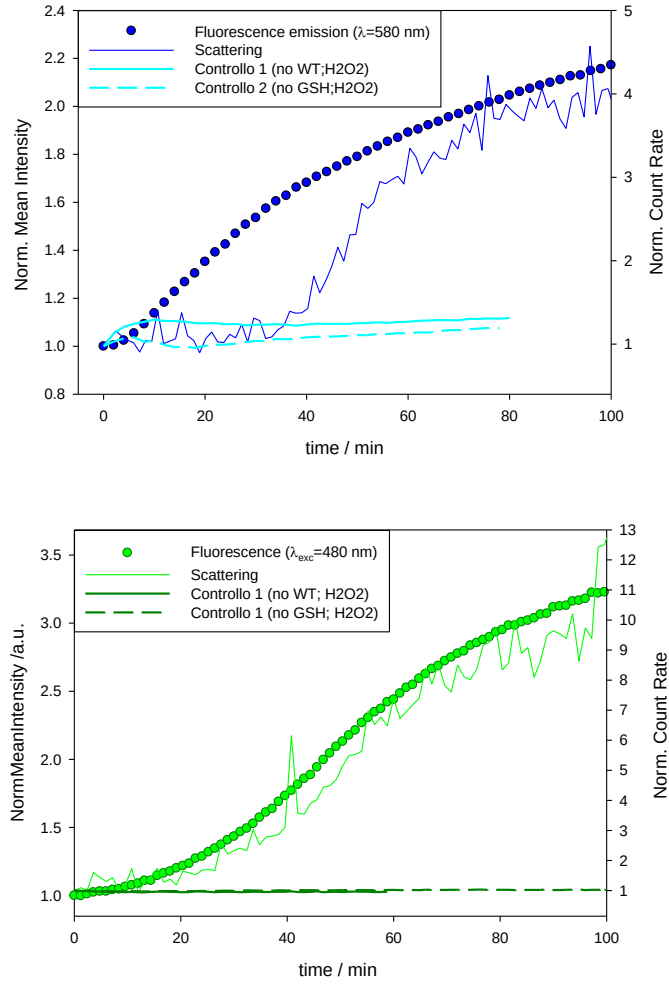

Fig. 3.6 *– In the graph are reported the fluorescence signal, scattering signal from DLS, and fluorescence control experiments for the protein aggregation kinetic of HA-RB GAPC1 and Tht-GAPC1 respectively, both in presence of NaCl at 25 °C.*

We observed, similarly to the previous experiments, that HA-RB shows a distinct fluorescence intensity increase at an earlier stage respect to DLS counts and to ThT confirming that, even at high NaCl concentration, HA-RB has a high affinity for early aggregates, which enhance the fluorescence quantum yield of initially self-quenched RB moieties. It is important to note that in the control experiments HA-RB does not show any intensity drift in the experimental conditions, even in presence of high NaCl concentration, and in presence of the redox chemical triggers H_2O_2 and GSH, or in presence of the protein without the redox chemical triggers (solid and dashed light blue lines in Figure 3.6).

This clear difference in the intensity trend at the beginning of the aggregation process represents an important preliminary assessment of the potential of HA-RB as a probe for early-stage aggregation.also compared to Tht (Figure 3.7)

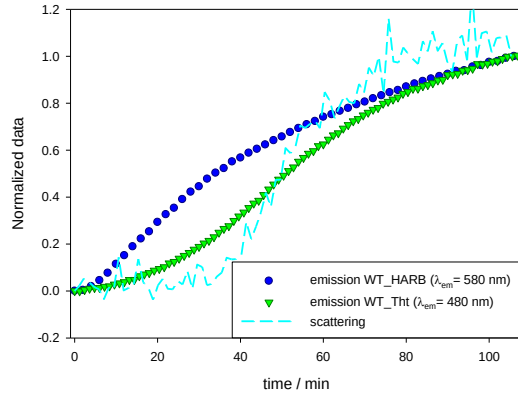

***Figure 3.7**– Fluorescence assay in cuvette comparing ThT and HA-RB, overlapped to DLS data of the aggregation process with NaCl.*

3.3.4 Fluorescence Microscopy: Laser scanning confocal microscopy

Going after the promising observations in the cuvette fluoresce assay, we decided to turn to fluorescence microscopy-based methods with the aim to gain deeper insight on the aggregation process and on the potential of the fluorogenic hyaluronan probe as diagnostic tool for early-stage aggregation.

Confocal microscopy allowed us to acquire different images of the aggregates at different stages of their aggregation.

Remarkably, at the beginning of the aggregation process the field of view appears homogenously dark with rare dim luminescent spots, proving that the initial state of HA-RB nanogels is effectively deeply quenched. The HA-RB nanostructures alone, therefore, do not interfere with the luminescence signal to be localized on the aggregation hotspots. After the lag-phase, we started to observe a relevant number of objects and soon this type of emissive aggregates starts to stick on one another, finally reaching the shape of the conglomerates that were previously observed via electron microscopy by the group of Prof. Zaffagnini (Figure 3.8).[21]

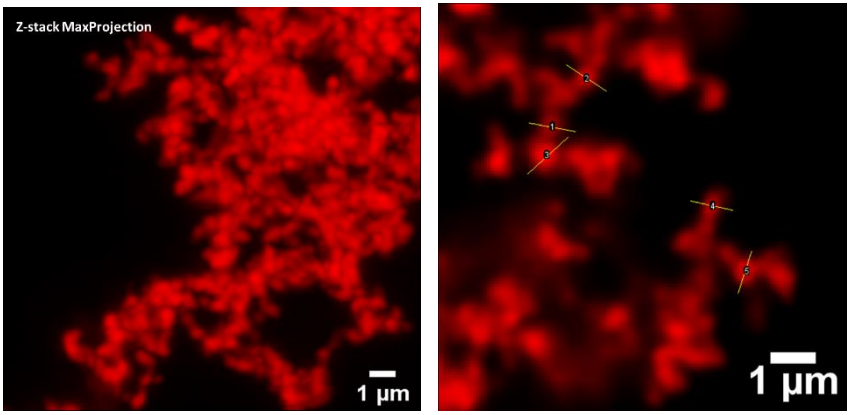

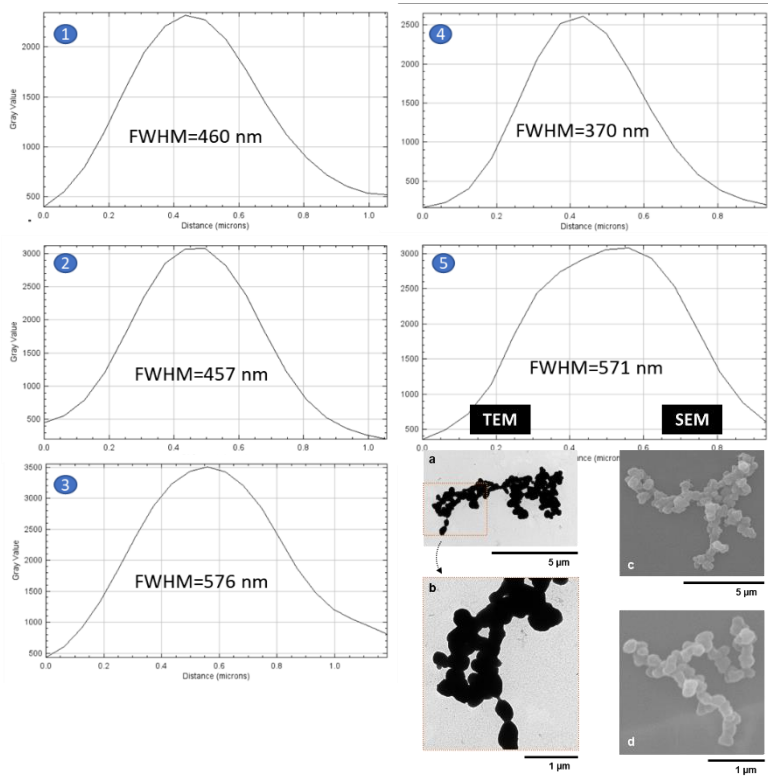

Fig. 3.8– *Max Projection of a Z-stack of late aggregates. Micrograph of globular-like aggregates from a zoomed region of the z-stack. TEM and SEM were taken by ref. [21]*

3.3.5 LASER-SHEET WIDE-FIELD MICROSCOPY and Nanotracking Particle Analysis experiment (NTA)

Accurate experiments at the confocal microscope revealed that the system features fast dynamics: misfolded proteins, oligomers and pre-aggregates diffuse rapidly in solution and cannot be imaged with our confocal setup; therefore, the acquisitions allowed us to make only qualitative observations on the early stage of the kinetics. In order to have quantitative insight on this complex environment we approached a technique – endowed with a better time resolution – which we implemented on a wide-field fluorescence microscope, that is based on laser-sheet excitation for out-of-focus fluorescence removal.

3.3.5.1 Calibration of the optical setup

Firstly, the homemade laser-sheet wide-field optical setup (described in the Methods section) has been calibrated using highly monodispersed polystyrene (PS) nanoparticles previously synthesized and available in our lab, having three different hydrodynamic diameters (90 nm, 150 nm, 170 nm). Each sample was diluted in a reduced volume quartz cuvette (500 μL) in a thermalised bath at 25°C. For each sample 1000 frames with exposure time of 35 msec (14 FPS) have been

acquired. After that, each acquisition has been analysed with the NanotrackJ plugin of ImageJ programme. In order to evaluate the analysis algorithm, during the analysis both the available methods , Walker's method (CIT) and Default Method, have been used for the distribution fitting. These results have been then compared to DLS measurement with very good agreement of the fitting data (Figure 3.8).

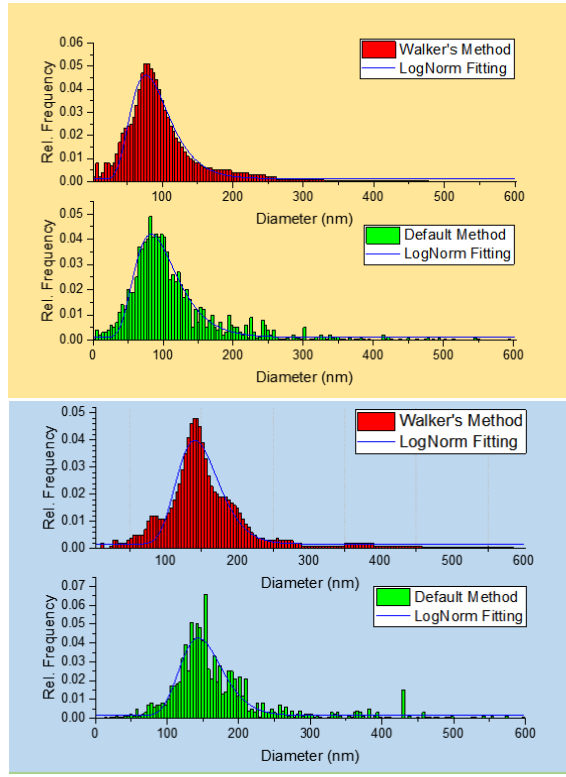

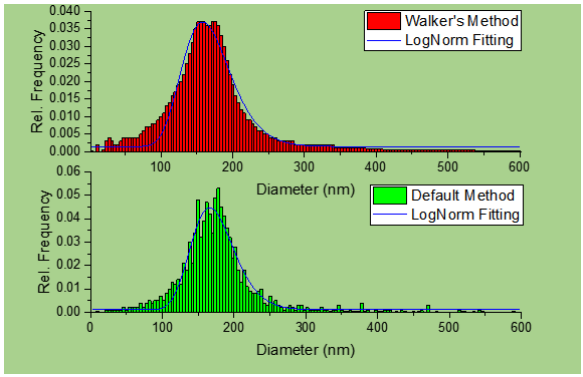

	DLS		NanoTracking (Laser Sheet)	
samples	dH	PDI	Walker Method	Standard Method
PS_1	80,52	0,107	87,03±0,71	94,26±0,71
PS_2	159,4	0,059	147,02±0,88	149,79±1,31
PS_3	179,1	0,123	165,39±0,78	172,41±0,78

Fig. 3.8 *– Dimensional distribution of the population of PS nanoparticles. The diameter values of the NTA analysis are in good agreement with the values in the table obtained with a DLS measurement.*

3.3.5.2 NTA aggregation experiment of GAPC1: early step detection

Encouraged by the fluorescence trend at the early step of the aggregation kinetics highlighted in the fluorescence assay in cuvette, we explored this region of the kinetic trace with a

NTA experiment. Since we were able to tune the lag-phase using the presence of high concentration of NaCl, we prepared the aggregation solution in a reduced quartz cuvette (500 μL) likewise in order to have a time window wide enough to acquire sufficient data. In this way we imaged the aggregation process (35 msec exposure time, 1000 frames) at different time steps which allowed us to capture the protein early aggregates diffusing at the early stages of formation. Combining the high signal-to-noise of the HA-RB probe and the calibrated optical setup, we were able to track clearly the diffusion of fluorescent aggregates in the early stage of the aggregation in the size range below the diffraction limit. After the acquisitions, we proceeded to analyse the different movies in order to calculate the trajectories of each object and retrieve from that the hydrodynamic range. We obtained in this way a distribution of diameters that can be calculate for each time step and monitoring the evolution of the size distribution during the lag-phase of the kinetic we can observe that the smallest size range (20 nm) appears in this phase and soon disappears in favour of a large population (Figure 3.9). In particular, the presence of a lag phase and the non- monodisperse distribution suggest a model of

aggregation compatible with a nucleation-controlled aggregation [23].

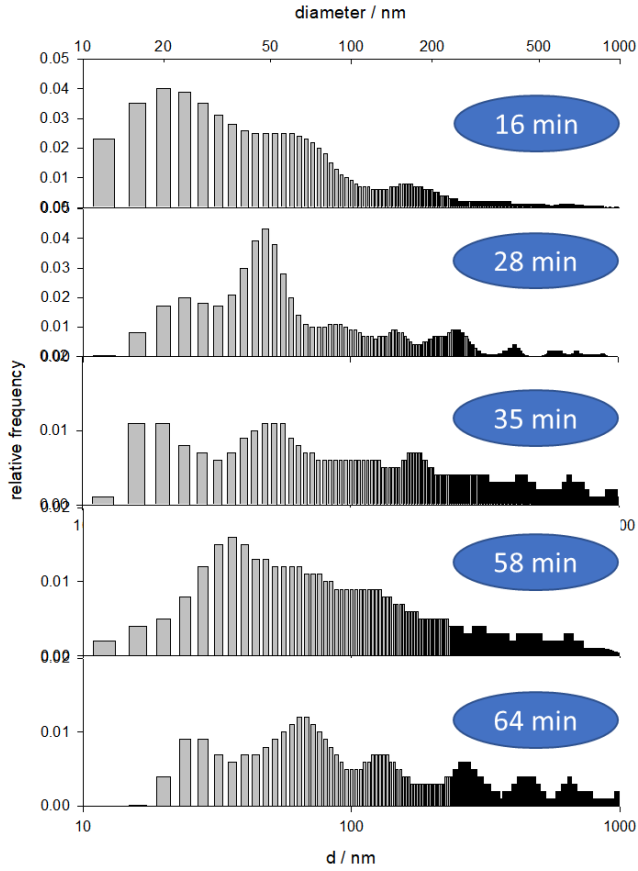

Fig. 3.9 *– Size distributions calculated from acquisitions at different time steps. Diameter axis is in logarithmic scale.*

3.4 Conclusions

In conclusion, we report the application of the fluorogenic HA-RB probe to monitor the aggregation process of the plant derived metabolic enzyme GAPC1 that occurs under oxidative stress. In particular, we highlighted the peculiar behaviour of the probe in the early steps of the aggregation kinetic which shows a rise in the fluorescence signal since the beginning, contrarily to what observed with DLS or with ThT, the golden standard to study aggregates of protein, which only display an increase of the signal after an initial – and "dark" – lag phase. These results suggest that HA-RB has a high affinity for early aggregates, which enhance the fluorescence quantum yield of initially self-quenched RB moieties. Affinity, indeed, is an important issue of other fluorescent of fluorogenic probes such as ThT, which, due to the low association constant, needs to be employed at rather high concentration (15-50 microM) [24] to push its association with protein aggregates. HA-RB, in comparison, could be used at extremely low concentration of hyaluronan chain (100 nM). Owing to the high-affinity interaction of HA-RB with the early aggregates, we were also able to further explore the lag-phase of the aggregation kinetic, which is otherwise difficult to investigate. We were able to

optimize a homemade optical setup for laser-sheet wide-field microscopy for nanoparticle tracking analysis (NTA). With this setup we managed to follow almost in real time the aggregation process of the protein showing a size distribution that shifts and broadens towards larger size values as the aggregation proceeds. Moreover, we demonstrated the possibility – with the present particle-by-particle method based on light-sheet microscopy and single particle tracking – to observe the size of the very early stage of aggregates at the single aggregate level thanks to the favourable fluorogenic photophysical properties of HA-RB and to its high affinity towards this type of aggregates. This represents a great advantage respect to previously reported approaches, such as those based on DLS measurements and on the use of ThT as fluorescent probe. These results suggest, together with the intrinsic versatility of the reported fluorogenic hyaluronan, that HA-RB probe could be a valid tool to investigate the elusive lag-phase of protein aggregation kinetics both in an easy way with a cuvette assay and also – with deeper insight yielding quantitative information – with laser sheet microscopy and NTA analysis.

REFERENCES

[1] A. Aguzzi, T. O'Connor, Protein aggregation diseases: Pathogenicity and therapeutic perspectives, Nat. Rev. Drug Discov. 9 (2010) 237–248. https://doi.org/10.1038/nrd3050.

[2] K. Nishitsuji, K. Uchimura, Sulfated glycosaminoglycans in protein aggregation diseases, Glycoconj. J. 34 (2017) 453–466. https://doi.org/10.1007/s10719-017-9769-4.

[3] L.J. Lapidus, Understanding protein aggregation from the view of monomer dynamics, Mol. Biosyst. 9 (2013) 29–35. https://doi.org/10.1039/c2mb25334h.

[4] D. Shi, A. Sheng, L. Chi, Glycosaminoglycan-Protein Interactions and Their Roles in Human Disease, Front. Mol. Biosci. 8 (2021) 1–15. https://doi.org/10.3389/fmolb.2021.639666.

[5] C.A. Ross, M.A. Poirier, Protein aggregation and neurodegenerative disease, Nat. Med. 10 (2004) S10. https://doi.org/10.1038/nm1066.

[6] M. Bucciantini, E. Giannoni, F. Chiti, F. Baroni, N. Taddei, G. Ramponi, C.M. Dobson, M. Stefani, Inherent toxicity of aggregates implies a common mechanism for protein misfolding diseases, Nature. 416 (2002) 507–511. https://doi.org/10.1038/416507a.

[7] S. Ziętkiewicz, K. Liberek, Dispose to the pole-protein aggregation control in bacteria, EMBO J. 29 (2010) 869–870. https://doi.org/10.1038/emboj.2010.12.

[8] A.J. Weids, S. Ibstedt, M.J. Tamás, C.M. Grant, Distinct stress conditions result in aggregation of proteins with similar properties, Sci. Rep. 6 (2016) 1–12. https://doi.org/10.1038/srep24554.

[9] E.W.J. Wallace, J.L. Kear-Scott, E. V. Pilipenko, M.H. Schwartz, P.R. Laskowski, A.E. Rojek, C.D. Katanski, J.A. Riback, M.F. Dion, A.M. Franks, E.M. Airoldi, T. Pan, B.A. Budnik, D.A. Drummond, Reversible, Specific, Active Aggregates of Endogenous Proteins Assemble upon Heat Stress, Cell. 162 (2015) 1286–1298.

https://doi.org/10.1016/j.cell.2015.08.041.

[10] D.C. David, N. Ollikainen, J.C. Trinidad, M.P. Cary, A.L. Burlingame, C. Kenyon, Widespread protein aggregation as an inherent part of aging in C. elegans, PLoS Biol. 8 (2010) 47–48. https://doi.org/10.1371/journal.pbio.1000450.

[11] D.M. Walther, P. Kasturi, M. Zheng, S. Pinkert, G. Vecchi, P. Ciryam, R.I. Morimoto, C.M. Dobson, M. Vendruscolo, M. Mann, F.U. Hartl, Widespread proteome remodeling and aggregation in aging C. elegans, Cell. 161 (2015) 919–932. https://doi.org/10.1016/j.cell.2015.03.032.

[12] L. Nover, D. Neumann, G. Democratic, Formation of Cytoplasmic, Mol. Cell. Biol. 3 (1983) 1648–1655.

[13] Y. Nakajima, S. Suzuki, Environmental stresses induce misfolded protein aggregation in plant cells in a microtubule-dependent manner, Int. J. Mol. Sci. 14 (2013) 7771–7783. https://doi.org/10.3390/ijms14047771.

[14] Y. Zhang, B. Ren, D. Zhang, Y. Liu, M. Zhang, C. Zhao, J. Zheng, Design principles and fundamental understanding of biosensors for amyloid-β detection, J. Mater. Chem. B. 8 (2020) 6179–6196. https://doi.org/10.1039/d0tb00344a.

[15] K.J. Cao, J. Yang, Translational opportunities for amyloid-targeting fluorophores, Chem. Commun. 54 (2018) 9107–9118. https://doi.org/10.1039/c8cc03619e.

[16] W. Wan, W. Jin, Y. Huang, Q. Xia, Y. Bai, H. Lyu, D. Liu, X. Dong, W. Li, Y. Liu, Monitoring the dynamics of proteome aggregation in live cells using a solubilized and noncovalent analogue of fluorescent protein chromophores, Anal. Chem. 93 (2021) 1717–1724. https://doi.org/10.1021/acs.analchem.0c04309.

[17] A. Aliyan, N.P. Cook, A.A. Martí, Interrogating Amyloid Aggregates using Fluorescent Probes, Chem. Rev. (2019). https://doi.org/10.1021/acs.chemrev.9b00404.

[18] P.C. Ke, E.H. Pilkington, Y. Sun, I. Javed, A.

Kakinen, G. Peng, F. Ding, T.P. Davis, Mitigation of Amyloidosis with Nanomaterials, Adv. Mater. 32 (2020) 1–7. https://doi.org/10.1002/adma.201901690.

[19] F. Xia, J. Wu, X. Wu, Q. Hu, J. Dai, X. Lou, Modular Design of Peptide-or DNA-Modified AIEgen Probes for Biosensing Applications, Acc. Chem. Res. 52 (2019) 3064–3074. https://doi.org/10.1021/acs.accounts.9b00348.

[20] T. Wang, N. Zhang, W. Bai, Y. Bao, Fluorescent chemosensors based on conjugated polymers with N-heterocyclic moieties: Two decades of progress, Polym. Chem. 11 (2020) 3095–3114. https://doi.org/10.1039/d0py00336k.

[21] M. Zaffagnini, C.H. Marchand, M. Malferrari, S. Murail, S. Bonacchi, D. Genovese, M. Montalti, G. Venturoli, G. Falini, M. Baaden, S.D. Lemaire, S. Fermani, P. Trost, Glutathionylation primes soluble glyceraldehyde-3-phosphate dehydrogenase for late collapse into insoluble aggregates, Proc. Natl. Acad. Sci. U. S. A. 116

(2019) 26057–26065.
https://doi.org/10.1073/pnas.1914484116.

[22] M. et al. Zaffagnini, TUNING CYSTEINE REACTIVITY AND SULFENIC ACID STABILITY BY PROTEIN MICROENVIRONMENT IN GLYCERALDEHYDE-3-PHOSPHATE DEHYDROGENASES OF ARABIDOPSIS THALIANA Mirko, Antioxid. Redox Signal. (2016) 502–517.
https://www.ptonline.com/articles/how-to-get-better-mfi-results.

[23] J. Philo, T. Arakawa, Mechanisms of Protein Aggregation, Curr. Pharm. Biotechnol. 10 (2009) 348–351.
https://doi.org/10.2174/138920109788488932.

[24] C. Xue, T.Y. Lin, D. Chang, Z. Guo, Thioflavin T as an amyloid dye: Fibril quantification, optimal concentration and effect on aggregation, R. Soc. Open Sci. 4 (2017).
https://doi.org/10.1098/rsos.160696.

CHAPTER 4

Characterization of nanomaterials through non-specific interactions of HA-RB probe with PAINT super resolution microscopy technique.

Research Activity at Nanoscopy for Nanomedicine group at the Eindhoven University of Technology, The Netherlands.

4.1 Introduction

Super resolution microscopy can be a formidable tool to explore and study properties of different nanomaterials. In this microscopy field we can find a wide range of techniques all of them with the capability to reach a resolution of few nanometres with single molecule sensitivity and multiple colours. Most of the approaches that can be found in literature, both diffraction limited and super -resolution ones, depend on a proper covalent labelling of the system with a fluorescent dye or a ligand/receptor couple to study the properties and the topography of a surface [1,2].This is a

major limitation for different application where super-resolution microscopy recently emerged as an interesting tool and where systems under analysis struggle to be easily functionalized with fluorescent moieties. For this reason, this chapter will focus on exploring the properties of the HA-RB probe that use non-specific interactions in order to have a reversible non-covalent absorption on the system surface/interface and whose fluorescent signal can be used for super resolution imaging. In particular, the polymeric probe will be used to study and characterize the topography of microplastics and other nanomaterials to show its possible use as a flexible tool for non-specific-interaction super-resolution imaging.

4.1.1 Optical light microscopy: the diffraction barrier

Contrary to electron microscopy techniques, in optical microscopy different optical setups are used to collect the light coming from the focal point of the objective. This approach is quite powerful since we can easily exploit a wide range of technique to have a fluorescent signal with a lot of information from the sample with low invasiveness, high penetration depth, chemical specificity, and easier sample

handling. However, one of the biggest physical limitations of these techniques is the diffraction limit of light. If we look at radiation as a propagating wave-packet through a lens, geometrically it cannot be focused on a single point, but it will give interference and will be smeared out over a region with a shape that has a full width at half maximum (FWHM) given by:

$$d = \frac{\lambda}{2n\,sin\alpha} \qquad \text{(eq.1.1)}$$

in the lateral plane and by:

$$\Delta z = \frac{2\lambda}{2n^2\,sin\alpha^2} \qquad \text{(eq.1.2)}$$

in the axial direction.

The FWHMs are governed by the wavelength of the radiation, λ, and the so-called numerical aperture of the lens $NA = 2n\,sin\alpha$ where n is the refractive index of the lens and α. the semi-aperture angle of the lens The theory describing the diffraction barrier has been formulated for the first time by Ernst Abbe in 1873 [3] and then mathematically demonstrated by Rayleigh in 1879 [4]. Consistently to the

equations 1.1 and 1.2, the shorter the wavelength, the smaller it is the power to resolve nanometric features. If we take into account radiation in the visible region of the electromagnetic spectrum ($\simeq$ 530 nm) and assuming NA = 1.25 of a standard 100x objective, we are not able to resolve features closer than 200 nm. Moreover, due to diffraction of light, the region over which the light is focused, which is called the point spread function (PSF), can illuminate hundreds of probes, exciting them all at the same time. Their fluorescence emission will be simultaneous, which will result in a hazy spot, and no accurate localization of individual fluorophores can be sort out. However, the high sensitivity, specificity and simplicity achievable with the fluorescence-based probes and systems encouraged the development of more spatially resolved techniques.

4.1.2 Beyond the diffraction limit

Firstly, if the propagation of the light emitted by the sample in an unconfined manner (far-field microscopy) experiences diffraction, one solution is to stay up close to the surface to collect the component of the light the does not undergo diffraction: the evanescent Near-field microscopy

circumvent the diffraction barrier by exploiting the unique properties of evanescent waves component [5,6]. Here, the light is confined by a sub-diffraction-sized aperture, and it propagates as an evanescent wave which exponentially decays within a distance $\ll \lambda/2$. Scanning the surface with the tip few nanometres away from the sample ($\ll \lambda/2$) results in spatial resolution higher than what can be achieved in far-field microscopy ($\ll$ 100 nm) [7,8]. However, near-field microscopy limits the investigation to surfaces, therefore the study of internal structures is not possible with this approach. Another technique relying on an evanescent wave is Total-internal-reflection fluorescence (TIRF) microscopy. In TIRF microscopy, only a thin layer of the sample can be illuminated varying slightly the illumination angle, leading to an efficient suppression of background fluorescence, less blurry images and sufficient depth of illumination [9] achievable with particular objective and lenses. Together with the instrument implementation, there is the need to exploit the photo-physical properties of the dyes to tune the number of the emitting point within the illumination volume to overcome the diffraction limit. Two different method have been developed: modulation of the effective PSF to shrink the illumination volume (coordinate-targeted methods) and

temporal separation of fluorophores (coordinate-stochastic methods) [10,11]. In coordinate targeted methods, a patterned illumination is used, such that the size of the effective PSF is reduced, and only a smaller number of molecules is excited. In coordinate-stochastic methods, single molecules are forced to emit at a relatively low density such that they are separated by a distance ≫ 200 nm in each frame. This enables precise single localization among molecules within the diffraction limited illumination volume. The term 'stochastic' refers to the random switching between the ON and OFF states of the fluorophores and ensures that the probability of finding two emitters closer than the diffraction limit at the same time in the ON state is very low. The central concept of this methods relies on temporal separation of the dyes: during all the acquisition time the distance between them must be tuned to be larger than the diffraction limit at any time point. Hence, if this condition is satisfied, the diffraction limited spot of the emitting event of each dye is analysed, the intensity profile modelled with a 2D-Gaussian function and the centroid is calculated, corresponding to the more probable location of the emitter (Figure 4.1). This enables higher localization precision of emitters position compared to the diffraction limited image.

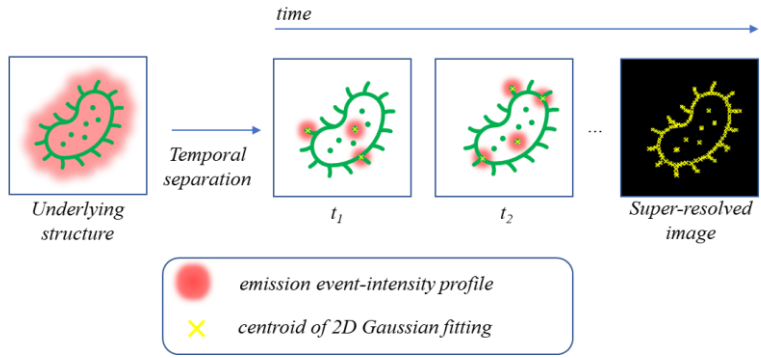

Fig 4.1 *- Principle of coordinate-stochastic methods.*

4.1.3 Coordinate-stochastic methods techniques

To achieve the temporal separation of the single fluorophores and to control the switching between the ON-state and OFF-state different mechanisms can be exploited. Depending on that mechanism, three main families of coordinate stochastic methods have been identified that go under the names of PALM [12], (d)STORM [13] and PAINT [14,15]. Moreover, variations with multiple colours and dimensional parameters of all these techniques have been developed and are known under a wide number of different acronyms. Concerning PALM microscopy, in this case proteins or organic dyes

having photo-activable fluorescence are used. Using an external stimulus – such as UV light – these fluorophores, initially in the dark state can be activated to an ON-state. For an efficient visualization, this technique requires that the majority of the emitters are in a stable OFF-state to achieve the blinking of the molecules [16]. The (d)STORM technique exploits fluorophores that can be reversibly switched between a fluorescent state singlet state and a non-fluorescent triplet state. To ensure the intersystem crossing (ISC) process towards the dark state, oxygen scavenger (i.e, glucose oxydase and catalase, protocatechuic acid) and reducing agents (i.e. 2-mercaptoethanol, mercaptoethylamine, L-Gluthathione) are commonly used. Then, high laser power brings the fluorophores back to the ON-state: with this process we have the blinking events [17]. Lastly, PAINT is a technique exploiting a transient binding of fluorescent dyes with the structure under investigation which can be specific or aspecific. When interacting, the dye motion is slowed down sufficiently to be localized, while fast diffusion in the unbound state precludes spurious single-molecule localizations. In particular, our experiments fall into this latter technique, using the blinking events generated by HA-RB probe fluorescence upon aspecific interactions with

different surfaces, thanks to its peculiar fluorescence mechanism.

4.2 Materials and methods

4.2.1 Microscopy

Images were acquired in a Nanoimager (ONI, Oxford) using the NimOS software. HA-RB was imaged with a 532 nm laser (25% power). The sample was illuminated using a total internal reflection fluorescence (TIRF) alignment system and the z-level was kept constant using the build-in perfect focus system. Fluorescence was recorded using ONI 100×, 1.49 NA oil immersion objective and passed through a quadband pass dichroic filter. Images were acquired onto a 425×518 pixels region (pixel size 0.117 μm) at 30 ms integration time for PAINT imaging. For the images were acquired 10.000 frames: Individual point-spread function (PSF) was fitted with a 2D gaussian function on the NimOS software to obtain the reconstructed super-resolved image. Data were then exported and the drift corrected with Thunderstorm plugin for Imagej when needed. Fourier Ring Correlation (FRC) [18,19]

plugin on ImageJ was used to assess the resolution of the samples features.

4.2.2 Sample preparation

Sample chambers consist of a coverslip (Menzel Gläser, 76 × 26 mm, thickness 1 mm) onto which a coverslip (Menzel Gläser, no. 1.5, 24 × 24 mm, thickness 170 μm) is glued with double-sided tape. Prior to assembly of the chamber, the coverslip is cleaned to remove impurities and reduce background fluorescence with a plasma gun treatment of 60 seconds.

Lab-grade plastic "PTFE" poly(tetrafluoroethylene) 9002-84-0 was purchased from Sigma Aldrich: the microplastic sample was already in powder form and were finely ground in a mortar to further reduce mesh size and increase the fraction of nanoplastics and small microplastics. In order to have a homogenous dispersed sample, as aforementioned in chapter 2, three different viscous solution of hyaluronan hydrogel (16 mg mL^{-1} native HA 200–600 kDa in water) were prepared using HA-RB solutions of 0.5 nM, 10 nM, and 70 nM. PTFE microplastic were dispersed in these solutions

and then a drop is deposited on the glass slide before closing the chamber.

4.3 Results and discussion

To evaluate the possibilities and limitations of PAINT as a complementary tool to visualize interfaces and their features we prepared three viscous solutions of HA-RB at 0.5 nM, 10 nM and 70 nM. 10,000 frames have been acquired for each sample, except for the lowest concentration (0.5 nM) which immediately showed a low count rate and a fast bleaching of the probe being impossible to register an image (Figure 4.2).

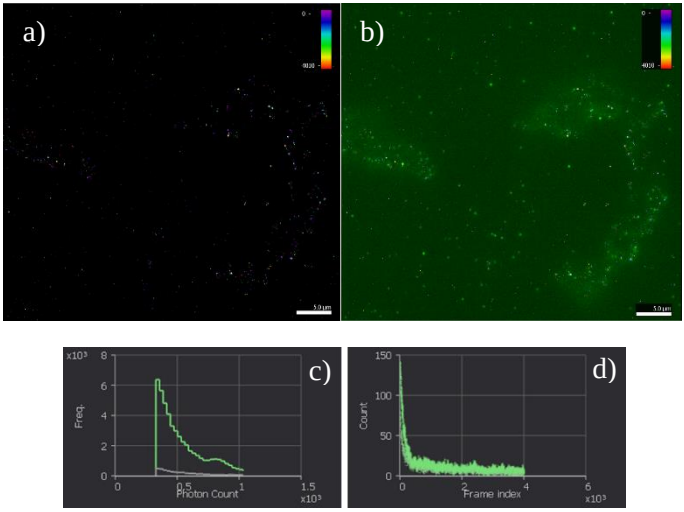

Fig. 4.2 *–(a) reconstructed images with poor number of localizations. (b) maximum intensity projection superimposed with the localization of the reconstructed image. (c) and (d) counts rate and frame index respectively.*

On the other hand, for the sample of PTFE with HA-RB 10 nM we were able to collect 10,000 frames with optimal blinking of the fluorophore (9×10^4 photon counts; stable signal after a starting moderate bleaching) and to retrieve calculated localizations image (Figure 4.3).

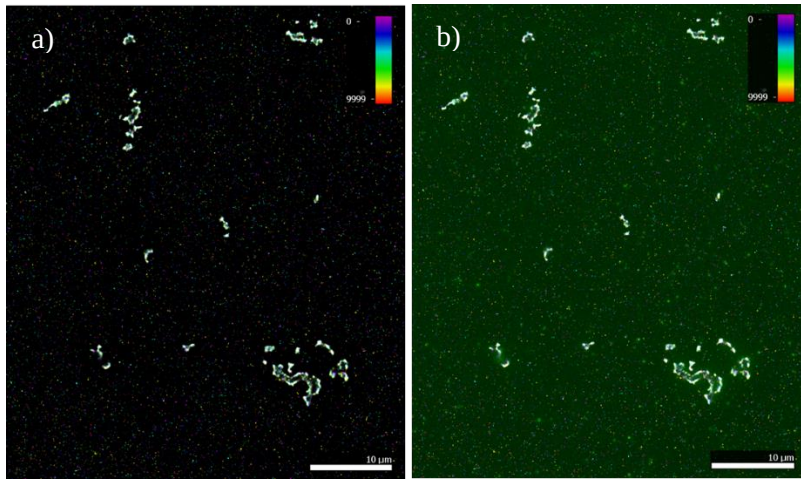

Fig. 4.3 *–a) Reconstructed images with high number of localizations for the sample PTFE with HA-RB 10 nM (uncertainty for single events*

is σ =14.04 ± 0.16). b) Maximum intensity projection superimposed with the localization of the reconstructed image.

In this case, the interaction of the probe colocalizes its fluorescence events on the hydrophobic zones of the surface of the PTFE debris highlighting its features. To evaluate the resolution of these features we applied a Fourier Ring Correlation based algorithm called FIRE [18,19] to the localization image, which can give an estimation of the resolved dimension of the objects based on the reconstructed image (Figure 4.4). The value calculated by the algorithm is equal to 265.11 nm and this value is consistent with few micrograph extrapolated from the image in order to test the goodness of the image analysis and calculation procedure (Figure 4.4 c-d).

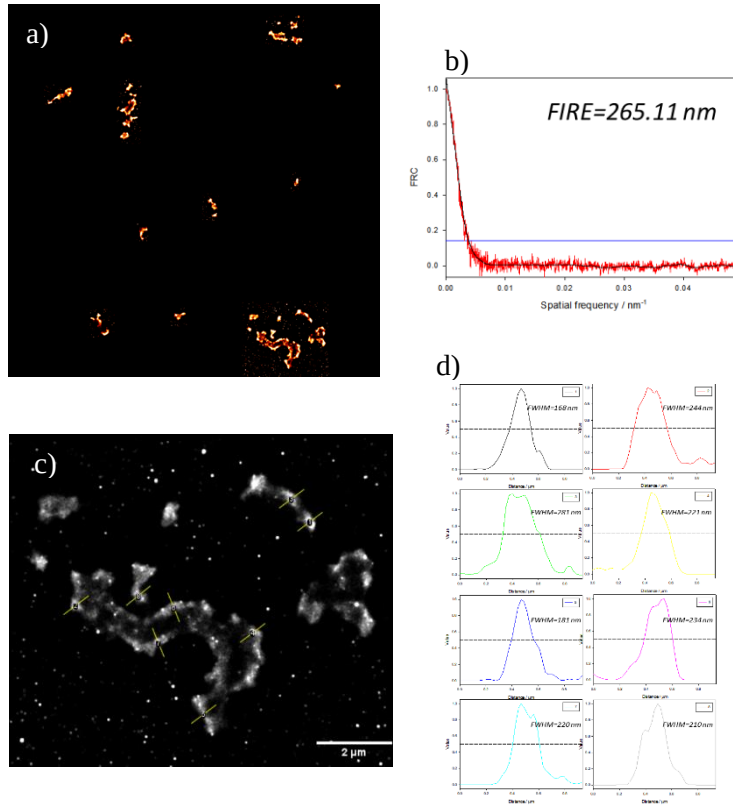

Fig. 4.4 *– In a) is reported the Fourier Ring Correlation image calculated by the algorithm. In b) is reported the FRC spatial frequency analysis: intercept of the line with the curve correspond to the resolution value in diameter calculated with the FIRE plugin in the real space .In c) and d) are reported the micrograph and the relative value of the FWHM.*

For the same glass slide we acquired a different field of view with the same idea and reported in Figure 4.5. In this case applying the FIRE algorithm we obtain a resolution value of 165.56 nm and also in this case consistent with individual micrograph extracted from the image.

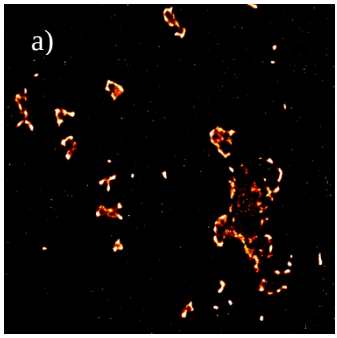

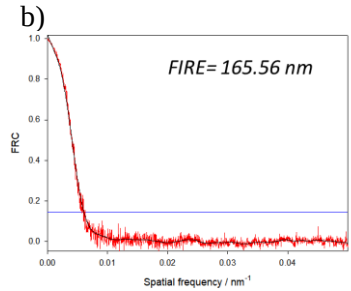

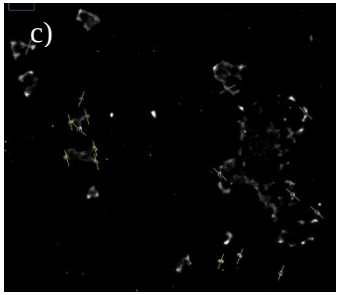

d)

Profile label	FWHM / nm
1	208
2	157
4	215
5	160
6	130
7	186
8	226
9	140

Fig. 4.5 *– In a) is reported the Fourier Ring Correlation image calculated by the algorithm. In b) is reported the FRC spatial frequency analysis: intercept of the line with the curve correspond to the resolution value in diameter calculated with the FIRE plugin in the*

real space. In c) and d) are reported the micrograph and the relative value of the FWHM.

The difference in the FIRE value of the two images can easily be linked to the polydispersity of the grinded sample and can already suggest the capability of the probe to interact successfully with a complex system in terms of surface characterization. Further to that, for the image relative to the last sample involving PTFE with HA-RB 70 nM we obtain similar results. For this sample the photon count rate is higher (2.3×10^5) and the blinking is extremely stable during all the acquisition. Also in this case the localization reconstruction image has been analysed with the FIRE algorithm revealing details of the surface with a resolution under 100 nm (Figure 4.6).

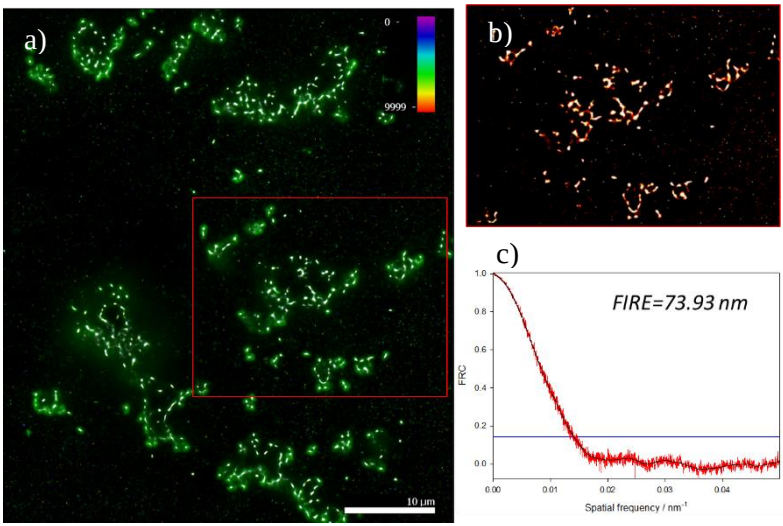

Fig. 4.6 *–In a) is reported the reconstructed images with high number of localizations for the sample PTFE with HA-RB 70 nM (uncertainty for single events is* $\sigma = 8.53 \pm 0.26$*). In b) is reported the Fourier Ring Correlation image calculated by the algorithm. In c) is reported the FRC spatial frequency analysis: intercept of the line with the curve correspond to the resolution value in diameter calculated with the FIRE plugin in the real space.*

Encouraged by the stability of the signal, we acquired also another field of view of this sample to make a fluorescence recovery after bleaching experiment (FRAP) and check if the probe in this case was adsorbed on the surface. In order to this measure we started the acquisition with the same

parameters of the other measures (25 % laser power, exposure time 30 ms) acquiring 1000 frames. After the 1000th frame, we raised the laser at its maximum power to ensure a fast and effective bleaching acquiring the signal for 500 frames. After that, we acquired again 1000 frames with parameters of the first step (Figure 4.7).

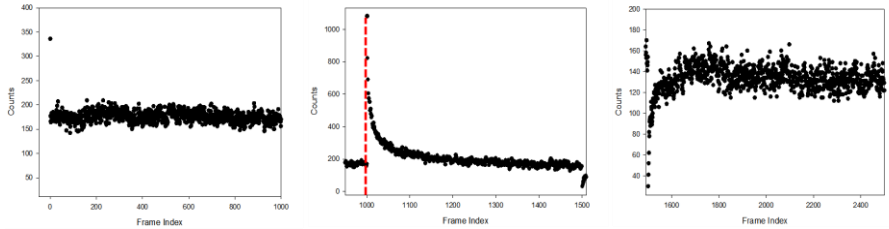

Fig. 4.7 *– Split plots of the three FRAP measure acquisition.*

Interestingly, the experiment shows that the probe is not adsorbed on the surface but instead continuously exchange between the surface and the solution which act as a large reservoir with a stable resistance to photobleaching in with normal acquisition parameter. This interesting behaviour could enable longer acquisition time improving also the localization of a large number of individual probes which improves the total resolution of the image.

4.4 Conclusions

In summary, we have introduced a promising new probe tailored to investigate surfaces through aspecific interactions without covalent labelling of the surfaces. Moreover, we can notice – comparing the images at different concentration of the HA-RB probe – that rising the concentration improves the conditions for an optimal blinking and photo-bleaching stability. For this type of super resolved technique that relies on temporal separation of the emitting events, the concentration should be kept really low in the 5 to 0.5 nM range. The reason why we observe quite the contrary must be reconducted to the polymeric nature and peculiar fluorescence mechanism of the HA-RB probe which balance the self-quenching of the emitting dye with the driving force of non-covalent interaction with the surfaces. This is also highlighted by the FRAP experiment demonstrating a continuous exchange at the interface between surface-bound and freely diffusing polymer chains functionalized with the fluorescent moieties. Thanks to these properties we were able to resolve surface details of complex and polydisperse samples under the diffraction limit (~250 nm). This preliminary research showed the potentiality of a flexible super-resolution tool with a non-labelling imaging approach

that could find many applications in different fields including interfaces study, soft matter characterization and nanotechnology.

4.5 References

[1] L. Woythe, P. Madhikar, N. Feiner-gracia, C. Storm, L. Albertazzi, A Single-Molecule View at Nanoparticle Targeting Selectivity: Correlating Ligand Functionality and Cell Receptor Density, (2022). https://doi.org/10.1021/acsnano.1c08277.

[2] L. Woythe, M.M.E. Tholen, B.J.H.M. Rosier, L. Albertazzi, Single-Particle Functionality Imaging of Antibody-Conjugated Nanoparticles in Complex Media, ACS Appl. Bio Mater. (2022). https://doi.org/10.1021/acsabm.2c00830.

[3] E. Abbe, Beiträge zur Theorie des Mikroskops und der mikroskopischen Wahrnehmung: II. Die dioptrischen Bedingungen der Leistung des Mikroskops, Arch. Für Mikroskopische Anat. 9 (1873) 418–440. https://doi.org/10.1007/BF02956174.

[4] Rayleigh, XXXI. Investigations in optics, with special reference to the spectroscope , London, Edinburgh, Dublin Philos. Mag. J. Sci. 8 (1879) 261–274. https://doi.org/10.1080/14786447908639684.

[5] M. Oheim, D. Loerke, R.H. Chow, W. Stühmer, Evanescent-wave microscopy: A new tool to gain insight into the control of transmitter release, Philos. Trans. R. Soc. B Biol. Sci. 354 (1999) 307–318. https://doi.org/10.1098/rstb.1999.0382.

[6] D. Axelrod, Evanescent excitation and emission in fluorescence microscopy, Biophys. J. 104 (2013) 1401–1409. https://doi.org/10.1016/j.bpj.2013.02.044.

[7] E. Betzig, R.J. Chichester, F. Lanni, D.L. Taylor, Near-field fluorescence imaging of cytoskeletal actin, Bioimaging. 1 (1993) 129–135. https://doi.org/10.1002/1361-6374(199309)1:3<129::AID-BIO1>3.3.CO;2-#.

[8] V. Walhorn, J. Paskarbeit, H.G. Frey, A. Harder, D. Anselmetti, Distance dependence of near-field fluorescence enhancement and quenching of single quantum dots, Beilstein J. Nanotechnol. 2 (2011) 645–652. https://doi.org/10.3762/bjnano.2.68.

[9] M. Oheim, A. Salomon, A. Weissman, M. Brunstein, U. Becherer, Calibrating Evanescent-Wave Penetration Depths for Biological TIRF

Microscopy, Biophys. J. 117 (2019) 795–809. https://doi.org/10.1016/j.bpj.2019.07.048.

[10] C. Eggeling, K.I. Willig, S.J. Sahl, S.W. Hell, Lens-based fluorescence nanoscopy, Q. Rev. Biophys. 48 (2015) 178–243. https://doi.org/10.1017/S0033583514000146.

[11] J.A.J. Fitzpatrick, Y. Inouye, S. Manley, W.E. Moerner, From “there’s plenty of room at the bottom” to seeing what is actually there, ChemPhysChem. 15 (2014) 547–549. https://doi.org/10.1002/cphc.201400097.

[12] S. Van De Linde, Single-molecule localization microscopy analysis with ImageJ, J. Phys. D. Appl. Phys. 51 (2019). https://doi.org/10.1088/1361-6463/ab092f.

[13] J. Xu, H. Ma, Y. Liu3, stochastic optical microscopy (STORM), Curr. Protoc. Cytom. 15 (2018) 477–491. https://doi.org/10.1002/cpcy.23.Stochastic.

[14] A. Aloi, N. Vilanova, L. Albertazzi, I.K. Voets, IPAINT: A general approach tailored to image the topology of interfaces with nanometer resolution,

Nanoscale. 8 (2016) 8712–8716. https://doi.org/10.1039/c6nr00445h.

[15] P. Delcanale, L. Albertazzi, DNA-PAINT super-resolution imaging data of surface exposed active sites on particles, Data Br. 30 (2020) 105468. https://doi.org/10.1016/j.dib.2020.105468.

[16] D. Kim, K. Jeong, J.E. Kwon, H. Park, S. Lee, S. Kim, S.Y. Park, Dual-color fluorescent nanoparticles showing perfect color-specific photoswitching for bioimaging and super-resolution microscopy, Nat. Commun. 10 (2019) 1–10. https://doi.org/10.1038/s41467-019-10986-4.

[17] M. Heilemann, S. Van De Linde, M. Schüttpelz, R. Kasper, B. Seefeldt, A. Mukherjee, P. Tinnefeld, M. Sauer, Subdiffraction-resolution fluorescence imaging with conventional fluorescent probes, Angew. Chemie - Int. Ed. 47 (2008) 6172–6176. https://doi.org/10.1002/anie.200802376.

[18] R.P.J. Nieuwenhuizen, K.A. Lidke, M. Bates, D.L. Puig, D. Grünwald, S. Stallinga, B. Rieger, Measuring image resolution in optical nanoscopy, Nat. Methods. 10 (2013) 557–562.

https://doi.org/10.1038/nmeth.2448.

[19] M. Van Heel, M. Schatz, Fourier shell correlation threshold criteria, J. Struct. Biol. 151 (2005) 250–262. https://doi.org/10.1016/j.jsb.2005.05.009.

CHAPTER 5

General Conclusion

The peculiar characteristics of nanomaterials make them suitable for their use in a variety of fields. Indeed, lot of attention has given to the comprehension of the interactions and the relationship intercurrent between properties and structure of the nanomaterials in order to rationally design and fine tuning their properties. Indeed, they constitutes a powerful platform to be engineered with well known different techniques to implement bio conjugated systems, biocompatible polymer, releasable loading, fluorescent probes for optical sensing with rationally designed sensors. In particular, the possibility to tailor their interactions can give a sensors high selectivity toward a target analyte. In addition, the main challenges for a sensors cannot only rely on its fine sensitivity, selectivity and stability but also to envision their applicability in complex matrix and their ability to provide information about the system in an easy way. These aspects have attracted interest for the interaction potential of HA with nanomaterials in nanomedicine and environmental application.

During this PhD thesis, the behaviour of a fluorogenic hyaluron probe functionalised with rhodamine B (HA-RB) has been studied with the following aims:

i) to detect micro and nanoplastics in aqueous samples; we demonstrated that HA-RB can be an efficient probe also to obtain information on their dimensions and chemical nature,
ii) to monitor in real-time the formation of protein aggregates even at their early stage, being a promising probe for obtaining information on several neurodegenerative diseases,
iii) to add a new tool to characterize the surface of microplastics with super-resolution microscopy through non-specific interactions and thus in a simplified approach.

In the first part, we report that hyaluronic acid functionalized with rhodamine B (HA–RB), with a very weak fluorescence intensity in water, readily adsorbs onto the surface of various MNPs with a concomitant enhancement of brightness, making them fluorescent. With confocal microscopy, fluorescently stained MNPs are clearly visible with size as small as the resolution of a confocal microscope, with nanoplastic fragments of approximately 250 nm clearly

standing out of the background. This high sensitivity can be achieved due to the recovery of the fluorescence quantum yield of the RB moieties thanks to a hydrophobicity-induced unquenching mechanism together with a high affinity interaction with MNPs. Furthermore, FLIM microscopy revealed that the lifetime parameter can take profit of the different degree of hydrophobicity-induced unquenching of HA–RB on the surface of different microplastics, making possible the identification of the types of MNPs based on their fluorescence lifetime.

These results represent a promising study demonstrating an efficient interaction of the probe with MNPs with the possibility for to recognize their chemical nature. As future perspective, its applicability could be extended to the analysis of real MNP debris in environmental samples which still remains a difficult challenge.

In the second part, we report the application of the fluorogenic HA-RB probe with the aggregates of the plant derived metabolic enzyme GAPC1 that are forming under oxidative stress. We demonstrated the possibility offered by our probe to monitor the kinetic of protein aggregation at

their early stages, highlighting that this kind of information cannot be obtained neither from DLS scattering signals nor using ThT – a dye widely used to study aggregates of protein – which do not show an early rise of their signal. These results suggest that HA-RB has a high affinity for early aggregates, which enhance the fluorescence quantum yield of initially self-quenched RB moieties. Thanks to the interaction of HA-RB with the early aggregates we were also able to further explore the lag-phase of the aggregation kinetic which is usually difficult to investigate. We were able to optimize an homemade optical setup for laser-sheet wide-field microscopy for nanoparticle tracking analysis (NTA) which made us able to follow almost in real time a dimension distribution of small pre-aggregates shifting and widening as the aggregation kinetic proceeds.

These results suggest, together with the intrinsic versatility of the reported fluorogenic hyaluronan, that HA-RB probe could be a valid tool to investigate the elusive lag-phase of protein aggregation kinetics both in a spectrofluorimetric and easy way with a cuvette essay and also with deeper insight with laser sheet microscopy and NTA analysis to quantitative information.

Lastly, we exploit the versatility of HA-RB using it as possible probe for PALM super-resolution acquisition. The aim was to exploit a non-specific, flexible tool able to successfully interact with the surface of complex and polydisperse microplastics and able to resolve nanometric features. The probe showed really stable blinking of the emitting events, which is fundamental for the technique, even at high concentration. The reason can be explained with the peculiar mechanism behind the fluorescence emission of the probe which balance the self-quenching of the emitting dye with the driving force of non-covalent interaction with the surfaces. FRAP experiment also confirmed this observation demonstrating a continuous exchange at the interface between surface-bound and freely diffusing polymer chains functionalized with the fluorescent moieties.

Thanks to these properties we were able to resolve surface details of complex and polydisperse samples under the diffraction limit (~250 nm). This preliminary research showed the potentiality of HA-RB as a flexible super-resolution tool with a non-labelling imaging approach.

In conclusion, in this Ph. D. thesis I focused my attention on the study of the application of a fluorogenic hyaluronan probe for detection and characterization of different nanomaterials with different advanced microscopy techniques. Hence, It is highlighted the application flexibility of the probe in different environment which is linked to the intrinsic nature of the probe and its fluorescence mechanism. The results presented in this thesis prove that biocompatible water-soluble polymers properly functionalised are highly promising tools for sensing and detection of different analytes of medical and environmental concern. Therefore, my research represents an encouraging step towards the design and the study of application flexible optical sensor for advanced microscopy techniques for biomedical and environmental application.

APPENDIX -PRINCIPLE OF PHOTOPHYSICS

A.1 ELECTRONIC EXITED STATE, JABLOSNKY DIAGRAM

To introduce the applications which takes advantage of fluorescence processes is useful to shows the origin and the behaviour of an electronic exited state. Electromagnetic radiation and matter can interact in different ways. Photochemistry is interested in the conversion of the energy (hν) of a photon absorbed by a chemical species in electronic energy, causing the transfer of an electron toward an orbital possessing higher energy. The species turns from its electronic ground state A to an electronic excited state A*, which possesses a different electronic configuration:

$$A + h\nu \rightarrow A^*$$

This different electronic distribution causes the excited states of a chemical species to have physicochemical properties so different from those of the ground state that they can be considered different chemical species. For this reason, it is possible to define photochemistry as the chemistry of excited states. A photon can be absorbed and provoke the formation of an electronic excited state only if its energy hν exactly corresponds to the energy difference between the excited and

the ground state. Absorption electronic transitions occur in a time scale of the order of femtoseconds (10-15 s, Franck Condon Principle), creating excited states which are transient and can deactivate in different ways, shown in the Jablonski diagram (Figure 1). In this diagram electronic states (the singlets S0, S1 and the triplets T1 and T2) are represented by thicker lines. The distinction between states with different spin multiplicity is due to the fact that transitions between these states are partially not allowed. Thinner lines represent the vibrational levels of the electronic states. After the energy absorption and reaching an excited vibrational level of an S2 electronic excited state, the molecule goes rapidly (< 10-12 s) to the ground vibrational level of that excited state (vibrational relaxation); then internal conversion occurs, passing from the ground vibrational level of S2 to the isoenergetic vibrational level of S1, the electronic state at lower energy (< 10-12 s). Another vibrational relaxation is then observed toward the ground vibrational state of S1, and at this stage the excited molecule can deactivate in two ways:

1- non-radiative deactivation: the energy is released as vibrational energy generating heat. If this process occurs between two states with the same spin multiplicity we speak about internal conversion (10-12 -10-6 s), while if the states

have different spin multiplicity, we have intersystem crossing (10-11 -10-6 s). The successive vibrational relaxation leads in the first case to the ground vibrational level of S0, in the second case to that of T1;

2- Radiative deactivation: it is a process that generates luminescence, and it is defined fluorescence if it occurs between states with the same spin multiplicity, phosphorescence if it occurs between states with different spin multiplicity. Similarly, to S1, T1 can deactivate to S0 by radiative deactivation (phosphorescence, 10-4 -102 s) or by nonradiative deactivation (intersystem crossing, 10-3 -10 s, and successive vibrational relaxation to S0). Long-lived states such as T1 can undergo photochemical reactions, for example with oxygen, producing other chemical species. Generally speaking, since the time scale to decay to S1 and T1 are shorter than that necessary to pass from S1 and T1 to

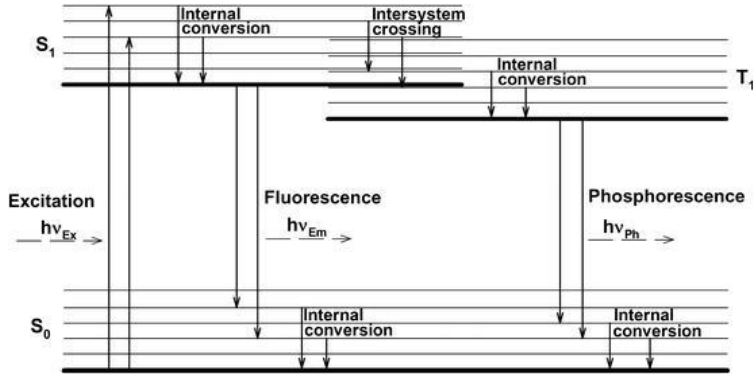

S0, only lowest energetic states of each spin multiplicity (that is S1 and T1) live enough to undergo luminescence (Kasha's rule) or photochemical reactions[1].

Fig. 1 - Jablonsky diagram for a generic molecule: horizontal lines symbolizes the vibrational levels in the electronic ground state (S0), in the first (lowest) excited singlet state (S1) and in the first excited triplet state (T1).Vertical arrows represent transitions between levels[2].

A.2 SOLVATOCHROMISM

Many relevant chemical and physical phenomena such as thermodynamics and reaction kinetics, as well as the position and intensity of the electronic absorption and emission bands, are often strongly dependent on the solvent. The basis of these effects on chemical equilibria and spectroscopic properties is the solvation of reagents and products. The solvation depends on the intermolecular forces between solute and surrounding solvent molecules, which include non-specific forces, such as electrostatic and polarization forces, and specific forces such as hydrogen bonds. The influence of solvents on the chemical equilibrium position was discovered in 1896 by Claisen and Wislicenus independently of each other. These results were examined by Stobbe, who in 1903 divided the solvents into two groups,

based on their ability to isomerize some tautomeric compounds, with subsequent subdivision in solvent donors of hydrogen bonds (HBD, protic solvents) and non-hydrogen

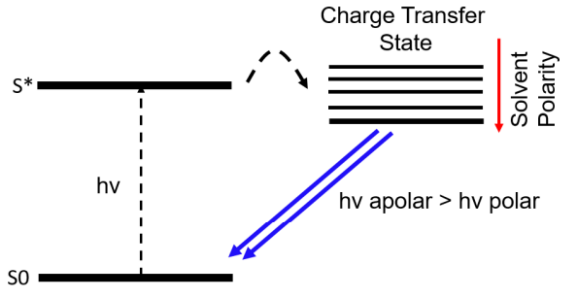

bond donors (non-HBD, aprotic solvents). Hantzschlater instead observed the displacement of the absorption and emission maxima at longer or shorter wavelengths of some molecules (fluorophores) as the polarity of the solvation environment varies.

Fig. 2 *– Jablonsky Schematization of Jablonsky diagram for a positive solvatochromic dye*

This phenomenon has taken the name of solvatochromism. The solvatochromism manifests itself in molecules having a different dipole moment for the ground state and the excited state. Solvents can therefore stabilize the two electronic states in a different proportion, thus varying the energy gap between them and therefore the energy of the transition. In general,

the transitions between two states, both in absorption and in emission, take place in a very short time, much lower than that of the motion of the nuclei, therefore considered to be stationary. Therefore, there is no reorganization of the solvent molecules causing the scheme of solvation of the excited state and that of the ground state to remain unchanged (Frank-Condon principle). However, if the residence time in an excited state is large enough, a reorientation of the solvent molecules can occur, with associated internal conversion, which brings the molecule into a lower energy vibroelectronic state and, from this new energy level, it can take place a radiative relaxation with fluorescence emission that brings the molecule to the ground state[3].In this case, the energy emitted by the solvatochromic dye molecule will be as low as the stabilization effect of the excited state operated by the solvent is greatest. There are two types of solvatochromism, negative and positive. If, as the solvent polarity increases, the fundamental state of the molecule is more stabilized than its first excited state, we observe hypsochromic shift (towards high energies in the spectrum) and the solvatochromism is called negative. Vice versa, if as the solvent polarity increases the excited state is stabilized more than the fundamental one, the solvatochromism is

called positive and we observe a batochromic shift (towards low energies). The solvatochromic probes are widely used for the study of polarity in complex systems or in the diagnostic field as bioluminescent sensors in imaging techniques[4], [5].

A.3 ELECTRONIC EXCITATION ENERGY TRANSFER

With the term electronic excitation energy transfer we indicate the process in which an excited molecule of a donor D* decays to its ground state D with the simultaneous transfer of its excitation energy to a molecule of acceptor A, which is thus led to an excited state A*:

$$D^*+A \rightarrow D+A^*$$

it is possible to observe this phenomenon exciting D in a spectral region in which it absorbs but A does not: if energy transfer occurs, D* emission is quenched and at the same time the appearance of the emission of A* is observed, which is called sensitized emission. In the case in which D and A are different molecules of the same chemical species we speak about homo energy transfer. It is possible to observe also intramolecular energy transfer in the case of a

(super)molecule containing a donor and an acceptor, separated by a spacer L:

$$D^*{-}L{-}A \rightarrow D{-}L{-}A^*$$

Two possible mechanisms of energy transfer exist, radiative one and non-radiative one. The radiative mechanism (also called trivial energy transfer) does not require the direct interaction of D and A, but it occurs via the electromagnetic field produced form the photons emitted by D, which can be absorbed by A, provided that an overlap between the emission spectrum of D and the absorption one of A exists. This mechanism consists of two different steps:

$$D^* \rightarrow D + h\nu' \text{ (Emission of the Donor)}$$

$$A + h\nu' \rightarrow A^* \text{ (Absorption of the Acceptor)}$$

It is possible to correlate the probability of absorption of A of a photon emitted by D*, that is the probability of energy transfer ($a_{D^* \rightarrow A}$), with the overlap between the emission spectrum of D and the absorption one of A. In particular a relation stands between $a_{D^* \rightarrow A}$ and the overlap integral J, defined as

$$J = \int_0^\infty F_D(\lambda)\varepsilon_A(\lambda)\lambda^4 \, d\lambda$$

where F_D is the normalized emission spectrum of D (the area under the spectrum is equal to 1) and $\varepsilon_A(\lambda)$ is the absorption

spectrum of A in $dm^3 \cdot mol^{-1} \cdot cm^{-1}$. So as *J* increases, the probability of radiative energy transfer linearly increases. This probability is also directly proportional to the concentration of A, to the optical path length and inversely proportional to the luminescence quantum yield of D. The radiative energy transfer can occur over extremely long distances: solar irradiation on Earth is a striking example. It is necessary that the transition of absorption in the acceptor is spin-allowed so that the radiative energy transfer can occur: thus singlet(D*)-singlet(A*) and triplet(D*)-singlet(A*) transfers are allowed, while singlet(D*)-triplet(A*) and triplet(D*)-triplet (A*) transfers are not allowed.

The non-radiative mechanism, on the other hand, requires an intermolecular interaction between D and A mediated by the electromagnetic field. The energy transfer between the partners occurs in resonance conditions, involving isoenergetic non-radiative transitions between D* and A. Also in this case the probability of energy transfer is directly proportional to *J*. The theoretical description of the process leads to obtain that the interaction between D* and A consists of a Coulombic term (Förster mechanism) and of an exchange term (Dexter mechanism) (Figure 3).

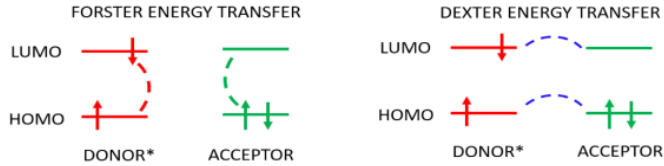

Fig. 3 *- energy transfer via Coulombic mechanism (left) and with exchange mechanism (right)*

The Coulombic mechanism arises from the coupling of the electronic transition moments of electric dipole of the transitions D*->D and A->A*. This interaction is governed by Förster's equation, which correlates the energy transfer kinetic constant with the distance R_{DA}:

$$k_{ET} = \frac{1}{\tau_D}\left(\frac{R_0}{R_{DA}}\right)^6$$

Where τ_D is the lifetime of the donor in the absence of the acceptor and R_0 is the Förster distance, that is the distance between D and \A at which the energy transfer rate (k_{ET}) is equal to the decay rate of the donor in the absence of the acceptor ($k_{ET}=1/\tau_D$). At this distance half of the molecules of D decay via energy transfer. Förster distance is correlated to the overlap between the emission spectrum of D and the absorption spectrum of A by means of the following relation:

$$R_0^6 = 2.303\frac{9000\chi^2\phi_D}{n^4 N_A 128\pi^5}J$$

Where χ is the orientational factor which describes the relative orientation of the electric dipole moment of D and A (it is assumed to be equal to 2/3 in the case of freely rotating D and A), Φ_D is the fluorescence quantum yield of D in the absence of A, n is the refractive index of the solvent, N_A is the Avogadro's constant, is the luminescence spectrum of D normalized to 1m and J is the spectral overlap. The higher the overlap between the emission spectrum of A and the absorption spectrum of A, the higher the value of R_0. Typical values are about 20-100 Å. It is possible to define an efficiency of energy transfer

$$\eta = \frac{k_{ET}}{k_{ET} + k_D}$$

which is linked to $R_{DA}^6$by means of the following relation

$$\eta = \frac{R_0^6}{R_0^6 + R_{DA}^6}$$

which highlights that the efficiency of the energy transfer process is equal to 0.5 when R_{DA}=R_0. It is possible to experimentally obtain η from the fluorescence quantum yield of D in the presence of A (Φ_{DA}) and in its absence (Φ_D), or from lifetimes in the two conditions (τ_{DA} , τ_D):

$$\eta = 1 - \frac{\Phi_{DA}}{\Phi_A}$$

$$\eta = 1 - \frac{\tau_{DA}}{\tau_A}$$

The processes of Förster type energy transfer are generally allowed if the transition in D and in A does not involve spin changes of the single species. On the contrary Dexter type energy transfer dominates. The exchange interaction requires a simultaneous double electronic exchange involving the LUMO of D and the HOMO of A (Figure 3) and it is a short-range interaction, becoming important when R_{DA} is ≤ 5 Å. According to Dexter model, the kinetic constant for the exchange mechanism decays exponentially with R_{DA} :

$$k_{ET}^{ex} = \frac{2\pi}{\hbar} K J^{ex} e^{\frac{2R_{DA}}{L}}$$

where K is a factor related to the specific orbitalic interaction, J^{ex} is the normalized overlap integral and L is an average Van der Waals radius which simulates molecular dimensions[6].

A4 ELECTRONIC ABSORPTION SPECTRA

For the acquisition of electronic absorption spectra, a double beam spectrophometer UV/Vis Perkin Elmer Lambda-45 was used. The amount of light absorbed is provided by the ratio of the intensity of incident light (I_0) and the intensity of transmitted light (I_t) and is expressed by Absorbance (A):

$A = log_{10} I_0 I_t$

$$A = log_{10} \frac{I_0}{I_t}$$

A is related to the chromophore concentration by the Lambert Beer equation as following:

$$A = c\varepsilon l$$

Where c is the chromophore concentration express in mol/L, ε is the molar extinction coefficient $(mol/L)^{-1}cm^{-1}$ and l is the optical path of the sample (1 cm optical path of the cuvette).

A5 LUMINESCENCE QUANTUM YIELD

The registration of the emission and excitation spectra were performed using a spectrofluorimeter Perkin Elmer LS55 and a spectrofluorimeter Edinburgh FLS920.

An important parameter to photophysically characterize samples is ttheir luminescence quantum yield (Φ_{PL}, QY), defined as the ratio between the number of emitted photons over the number of photons absorbed by a species at the same excitation wavelength:

$$\phi_{PL} = \frac{number\ of\ emitted\ photons}{number\ of\ absorbed\ photons}$$

A fast and useful method to determine the luminescence quantum yield is to compare the emission of a sample with a reference species having a known quantum yield, upon

excitation of both reference and sample at the same wavelength. The chosen reference has to emit in the same spectral region of the sample and the emission spectra must be recorded in the same experimental conditions. For the assessment of Φ_{PL} we adopted the following experimental procedure: the absorption spectra of the sample and of the reference were registered and, when possible, isoabsorption points were used as excitation wavelength for the registration of emission spectra. The following equation was used to determine the value of luminescence quantum yield:

$$\phi_{PL} = \phi_{ref} \frac{I_x}{I_{ref}} \frac{A_{ref}}{A_x} \left(\frac{n_x}{n_{ref}} \right)^2$$

Where Φ_{ref} is the fluorescence QY of the reference, I_{ref} and I_x are the emission intensities of the reference and the sample, respectively; A_{ref} and A_x are the absorbance at the excitation wavelength of the reference and the sample; n_{ref} and $nx$are the refractive index of the solvents.

A6 EXCITED STATE LIFETIME MEASUREMENTS

Excited state lifetime measurements were performed using a spectrofluorimeter Edinburgh Analytical Instruments FLS920, equipped with a time-correlated single-photon counting device, which is able to measure lifetimes in a range

between 0.5 ns and 30 μs. The time-correlated single-photon counting is based on the probability that a single photon emitted by a luminescent sample is collected by a proper high sensitivity detector: this probability is statistically correlated with the variation of the concentration of the excited states in solution.

A.7 DYNAMIC LIGHT SCATTERING

Dynamic Light Scattering (DLS) measurements were performed using a Malvern Instruments DLS ZetaSizer Nano-ZS. With this instrument it is possible to determine the dimension of particles having a diameter between 1 nm and 10 μm. It exploits the study of Brownian motions to determine the hydrodynamic diameter of particles suspended in solution. The hydrodynamic diameter is obtained by the correlation of the scattering intensity fluctuations recorded over time upon irradiation of the sample with a 633 nm laser. The Brownian motion of the particles is described by translational diffusion coefficient (D) that is related to the hydrodynamic diameter through the Stokes-Einstein's equation

$$\mathrm{d(H)} = \frac{kT}{3\pi\eta\mathrm{D}}$$

where d(H) is the hydrodynamic diameter, k is the Boltzmann constant, T is the temperature, η(T) is the viscosity of the solvent and D is the diffusion coefficient. Through this equation the hydrodynamic diameter, thus the diameter of a sphere having the same diffusion coefficient of the particles, can be obtained. The fluctuation of the intensity of the scattering produced in a short time-scale is analysed using the correlation function.

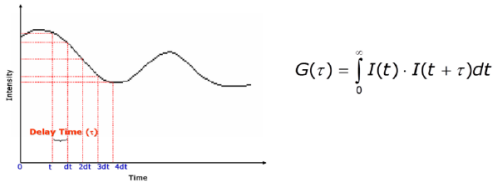

Fig. 4 *- Funzione di correlazione G, rappresentazione grafica e formula matematica*

The correlation indicates the degree of similarity of two measurements at different times. For particles of higher dimensions, the correlation will last for longer times than in the case of smaller particles.

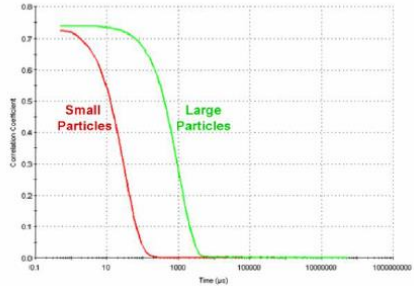

Fig. 5 *– trend of the correlation coefficient for large particles (green line) and small particles (red line) versus time*

The particle size distribution is obtained from the relative scattering intensity graph of the several particle size classes (intensity size distribution). It is also possible to obtain this distribution as a function of particle volume, or particle number. Let us consider, for example, a sample containing two populations of spherical particles having a diameter of 5 and 50 nm respectively and present in the same number (Figure 6). As far as the number of particle is concerned, the graph consists of two peaks, one at 5 nm and the other at 50 nm, with a 1:1 ratio. If we convert the number distribution in volume distribution, the two peaks ratio is 1:1000, because the volume of a sphere is equal to $\frac{4\pi}{3}\left(\frac{d}{2}\right)^3$. If we switch to

intensity distribution, the ratio becomes equal to 1:106 according to Rayleigh approximation.

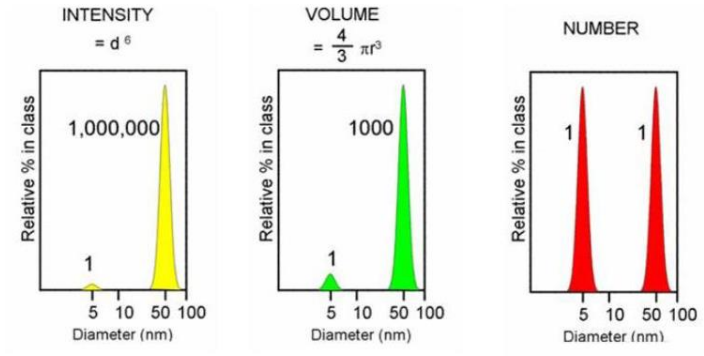

Fig. 6 *– number, volume and intensity distribution of a sample containing spherical particles of 5 nm and 50 nm diameter in equal numbers.*

A.8 LIGHT-SHEET MICROSCOPY FOR NANOPARTICLE TRACKING ANALYSIS (NTA)

The general principle of light sheet microscopy is that optical sectioning is achieved by illuminating the sample from the side with a thin sheet of laser light that will shine a relatively narrow plane of the sample. By shaping the light source in such way, light-sheet microscopy enables high temporal and spatial resolution offering high imaging speed, higher number of events acquisitions, reduced phototoxicity and

photobleaching if compared to other widefield and confocal techniques. In the light-sheet microscopy field we find the nanoparticle tracking analysis (NTA) which relies on spatial-temporal resolution of the Brownian Motion of the particles to calculate their equivalent hydrodynamic diameter. The theoretical base of the technique stems from the calculation of the trajectories of each single particle which can be achieved recording the movement of the particles in the illumination volume. From these trajectories we can calculate the mean square displacement to obtain the diffusion coefficient that can be related through the Stokes-Einstein equation to a sphere equivalent hydrodynamic radius:

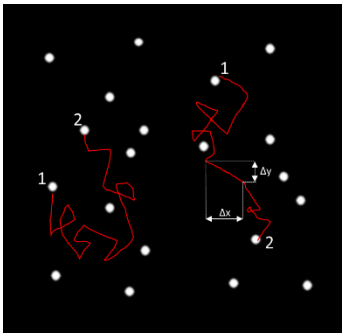

$$\frac{\left\langle \overline{(x,y)}^{\,2} \right\rangle}{4} = Dt = \frac{k_B T}{3\pi\eta d_h}$$

$\left\langle \overline{(x,y)}^{\,2} \right\rangle$ = *mean square displacement* D = *diffusion coefficient*

t = *sampling time* k_B = *Boltzmann constant*

η = *viscosity of the solvent* d_h = *hydrodynamic diameter*

The technique calculates particle size on a particle-by particle basis, overcoming the weaknesses in ensemble techniques such as dynamic light scattering that, for example, is quite

sensitive to the presence of large particles and huge differences in particle dimensions in polydisperse samples [7]. It is also worth to mention that this technique offers the possibility to monitor also the fluorescence signal from the particles allowing to investigate properties that are out of the DLS technique capability, i.e. accurate sizing, counting and phenotyping of biological relevant system such as extracellular vesicles [8].

REFERENCES

[1] M. Montalti, A. Credi, L. Prodi, and M. T. Gandolfi, *HANDBOOK OF PHOTOCHEMISTRY*, 3rd ed. Taylor & Francis Group, 2006.

[2] D. Okuno, R. Iino, and H. Noji, *Fluorescence: General Aspects. In: Roberts G.C.K. (eds) Encyclopedia of Biophysics. Springer, Berlin, Heidelberg*. Springer, 2013.

[3] E. Buncel and S. Rajagopal, "Solvatochromism and Solvent Polarity Scales," vol. 6, no. 9, pp. 226–231, 1990.

[4] L. Malacrida, D. M. Jameson, and E. Gratton, "A multidimensional phasor approach reveals LAURDAN photophysics in NIH-3T3 cell membranes," *Sci. Rep.*, no. July, pp. 1–11, 2017.

[5] O. Golfetto, E. Hinde, and E. Gratton, "Laurdan Fluorescence Lifetime Discriminates Cholesterol Content from Changes in Fluidity in Living Cell Membranes," *Biophysj*, vol. 104, no. 6, pp. 1238–1247, 2013.

[6] J. R. Lakowicz, *Principles of Fluorescence Spectroscopy*, 3th ed. Springer Nature.

[7] A. Kim, W.B. Ng, W. Bernt, N.J. Cho, Validation of Size Estimation of Nanoparticle Tracking Analysis on Polydisperse Macromolecule Assembly, Sci. Rep. 9 (2019) 1–14.

[8] R.A. Dragovic, C. Gardiner, A.S. Brooks, D.S. Tannetta, D.J.P. Ferguson, P. Hole, B. Carr, C.W.G. Redman, A.L. Harris, P.J. Dobson, P. Harrison, I.L. Sargent, Sizing and phenotyping of cellular vesicles using Nanoparticle Tracking Analysis, Nanomedicine Nanotechnology, Biol. Med. 7 (2011) 780–788